

FORMATION OF THE OXIDE FUME AND AEROSOL DISPERSAL FROM THE
OXIDATION OF URANIUM METAL AT TEMPERATURES LESS THAN 1000 °C

by

DOUGLAS KRISTOPHER CLARK

B.S., University of Kansas, 2001

A REPORT

submitted in partial fulfillment of the requirements for the degree

MASTER OF SCIENCE

Department of Chemical Engineering
College of Engineering

KANSAS STATE UNIVERSITY
Manhattan, Kansas

2009

Approved by:

Major Professor
Larry E. Erickson

COPYRIGHT

This document has been authored by a subcontractor of the U.S. Government under contract DE-AC05-00OR-22800. Accordingly, the U.S. Government retains a paid-up, nonexclusive, irrevocable, worldwide license to publish or reproduce the published form of this contribution, prepare derivative works, distribute copies to the public, and perform publicly and display publicly, or allow others to do so, for U. S. Government purposes.

DISCLAIMER

This work of authorship and those incorporated herein were prepared by Contractor as accounts of work sponsored by an agency of the United States Government. Neither the United States Government nor any agency thereof, nor Contractor, nor any of their employees, makes any warranty, express or implied, or assumes any legal liability or responsibility for the accuracy, completeness, use made, or usefulness of any information, apparatus, product, or process disclosed, or represents that its use would not infringe privately owned rights. Reference herein to any specific commercial product, process, or service by trade name, trademark, manufacturer, or otherwise, does not necessarily constitute or imply its endorsement, recommendation, or favoring by the United States Government or any agency or Contractor thereof. The views and opinions of authors expressed herein do not necessarily state or reflect those of the United States Government or any agency or Contractor thereof.

Abstract

The reaction chemistry of uranium metal has been well documented for use in the development of nuclear fuels. The oxidation of uranium from the thermal stress of nearby combustion is different than that of a reactor environment due to the selectivity of the various competing reactions. This work extracts available information in literature and various experiments over the last 60 years to provide a critical look at the response of uranium metal to thermal stress. The oxide fume formed and the equilibrium phase shifts during the dispersal of the airborne particulate are of principal interest when determining potential consequences to the health and safety of the workers, members of the public, and the environment. The transport phenomena and reaction kinetics of the oxide fume are also discussed at various distances from the source material.

Uranium is a versatile element that can form numerous compounds, of which the oxides are the forms that are most readily generated under thermal stress and also pose the largest health risk to human beings, primarily through inhalation. A general summary of uranium and the dry compounds (oxides and carbides) is provided discussing the different structures of each state. The reaction kinetics and selectivity as the oxidation progresses is discussed for typical uranium metal forms at temperatures above and below the ignition point. Characteristics of potential fires are qualified for determining thermal stress. The creation of the oxide fume is outlined followed by dispersal characteristics of the aerosol. These molecular processes are related to the release fractions of uranium under fire scenarios which are compared with available experimental data from the regulatory handbooks. A critical look at the conclusions of the handbook with recommendations for revising the existing guidelines and additional testing are made in the interest of ensuring that derived controls are appropriate to reduce the risk of accidents involving the oxidation of uranium metal.

Table of Contents

List of Figures	vii
List of Tables	viii
Acknowledgements	ix
Dedication	x
Preface	xi
CHAPTER 1 - Uranium, the Element and Dry Compounds	1
1.1. Uranium Metal (U)	2
1.1.1 Alpha Phase	2
1.1.2 Beta Phase	3
1.1.3 Gamma Phase	3
1.2. Uranium Monoxide (UO)	4
1.3. Uranium Monoxide to Dioxide Intermediates (UO _{1,x})	5
1.4. Uranium Dioxide (UO ₂)	6
1.5. Uranium Dioxide to Triuranium Octaoxide Intermediates (UO _{2,x})	7
1.6. Triuranium Octaoxide (U ₃ O ₈)	9
1.7. Uranium Trioxide (UO ₃)	10
1.8. Uranium Carbides (UC _x)	11
CHAPTER 2 - Reaction Kinetics at Various Temperatures	13
2.1. Normalization and Use of Specific Area (cm ² /g)	13
2.1.1 Nominal Forms of Uranium Metal Storage	14
2.1.1.1 Depleted Uranium Penetrators	14
2.1.1.2 Uranium Ingots and Billets	15
2.1.1.3 Reactor Foils	16
2.1.2 Nominal Forms of Uranium Metal Byproducts	16
2.2. Uranium Oxidation	17
2.2.1 Oxidation Below the Ignition Temperature	18
2.2.2 Oxidation Above the Ignition Temperature	27
2.2.3 Oxidation in the Transition Region	30

CHAPTER 3 - Fires Involving Uranium Metal	33
3.1. Combustion Product Interactions with Uranium Oxidation	33
3.1.1 Acceleration of Oxidation Reactions in the Presence of Carbon Dioxide.....	34
3.1.2 Retardation of Oxidation Reactions in the Presence of Carbon Monoxide.....	34
3.2. Potential Worst Case Fire Scenarios.....	35
3.3. Outlining of Zones Corresponding to the Ignition Region.....	36
3.4. Burn Rate Relationship to Specific Area.....	38
3.5. Maximum Oxidation of Uranium Forms.....	42
CHAPTER 4 - The Oxide Fume	43
4.1. The Creation of Oxide Particulate	43
4.1.1 The Progression of Oxidation Through Uranium Metal.....	44
4.1.2 The Impacts of Density Changes Associated With the Oxidation of Metal.....	44
4.1.3 Crystalline Structure Impacts on the Oxidized Metal.....	46
4.1.4 The Relationship Between Pyrophoricity and Aerosol Generation.....	47
4.2. Equilibrium of the Aerosol	48
4.2.1 The Relationship Between Structure and Temperature of Oxidation.....	48
4.2.2 The Associations Between D_{AE} and Oxidation State.....	49
4.2.3 The Reactions of the Oxide Fume as Temperature Decreases	50
4.2.4 Characteristics of the Aerosol at Equilibrium.....	51
CHAPTER 5 - Initial Dispersion of the Oxide Fume.....	53
5.1. Gaussian Dispersion at Distances Less Than 100 Meters from the Origin	53
5.2. Gravimetric Settling / Dry Deposition of the Particulate	55
5.3. Cooling of the Oxide Fume at Distances Less Than 100 meters.....	56
5.4. Changes in the Oxide Fume as Temperature Drops Below 100 °C.....	57
5.5. Summary of Dispersion Impact When Determining Initial Oxide Fume.....	58
CHAPTER 6 - Application of Release Fractions	59
6.1. Review of the Experiments and Conclusions of DOE-HDBK-3010-94	59
6.2. Analysis of the Bounding ARF/RF Values From Carter and Stewart.....	61
6.3. Analysis of the Maximum ARF/RF Values From Elder and Tinkle	62
6.4. Analysis of the Primary ARF/RF Values From Elder and Tinkle.....	66
6.5. Recommendations of ARF/RF Values Based on Specific Area.....	67

CHAPTER 7 - Conclusions Regarding Uranium Release Fractions.....	69
7.1. Recommendations for the Revision of DOE-HDBK-3010	69
7.2. Considerations for Future Testing.	71
7.3. Closing Summary	72
References	73
Appendix A - Physical Properties of Uranium	A-1
A.1 Mechanical Properties of Uranium Metal.....	A-1
A.2 Chemical Properties of Uranium Metal	A-1
Appendix B - Data for Figure 2.1	B-1

List of Figures

Figure 1.1 Face Centered Cubic Fluorite Structure of UO_2 [Allen and Tempest (1986)]	6
Figure 1.2 Comparison of Structures of UO_2 to U_3O_8 [Allen and Tempest (1986)]	9
Figure 1.3 Comparison of Orthorhombic $\gamma\text{-UO}_3$ to Fluorite UO_2 [Allen and Tempest (1986)]..	10
Figure 2.1 Relationship Between Specific Area and Uranium Ignition. [Baker et al (1966)].....	18
Figure 2.2 Unoxidized Uranium Reference Diagram.	19
Figure 2.3 Uranium Monoxide Layer Formation.	19
Figure 2.4 Uranium Skin Formation.	20
Figure 2.5 UO_2 Layers and Surface Roughness.....	21
Figure 2.6 UO_2 Surface Image [Mishima et al (1985)]	21
Figure 2.7 Arrhenius Plot for $\text{UO}_{2,x}$ Formation on UO_2 [McEachern and Taylor (1997)]	22
Figure 2.8 Uranium Dioxide Intermediates	23
Figure 2.9 $\text{UO}_{2,x}$ Surface Image [Mishima et al (1985)].....	23
Figure 2.10 Formation of the U_3O_8 Oxide Layer.....	24
Figure 2.11 U_3O_8 Surface Image [Megaw et al (1961)]	25
Figure 2.12 Phase Diagram for U-O at 1 Bar [Guéneau et al (2002)].	25
Figure 2.13 Temperature Profile After Uranium Ignition [Baker et al (1966)].....	27
Figure 2.14 Uranium Oxidation Above & Below Ignition Temp [Baker and Bingle (1966)]	28
Figure 2.15 Cumulative Distribution of Particulate Size Above & Below Ignition.....	29
Figure 2.16 UC_x Cracks in UO_2 Layers [Stobbs and Whittle (1966)].....	31
Figure 2.17 UC_x Cracks in U_3O_8 Layers [Stobbs and Whittle (1966)].....	32
Figure 4.1 Uranium Oxidation Profile at Constant Gas Temp. [Isaacs and Wanklyn (1960)]	46
Figure 4.2 Particulate Size Distribution in Human Lungs [Tisch (2006)].....	51
Figure 5.1 Gaussian Dispersion Model.....	54
Figure A.1 Density Change in the UO_2 to U_3O_8 transition.....	A-1

List of Tables

Table 1.1 Selected Thermodynamic Properties of Uranium & Oxides (Pure)	8
Table 1.2 Summary of Crystalline Structures of Selected Uranium Compounds	11
Table 2.1 Specific Area for Depleted Uranium Penetrators	15
Table 2.2 Specific Area for Typical Uranium Ingots and Billets	15
Table 2.3 Selected Thermodynamic Data of Uranium & Oxides at 298.15 K	26
Table 2.4 Heat Capacities of Uranium Oxides [Grenthe et al (2004)]	26
Table 3.1 Fire Scenario Heat Characteristics.....	37
Table 3.2 Controlled Temperature, in Air, Results From Elder and Tinkle (1980)	40
Table 3.3 Controlled Temperature, with CO ₂ , Results From Elder and Tinkle (1980).....	40
Table 3.4 Uncontrolled Temperature Results From Elder and Tinkle Experiments (1980).....	41
Table 3.5 Example Burn Durations for a Burn Rate of 0.152 cm/h.	41
Table 3.6 Maximum Oxidation of Uranium Forms	42
Table 6.1 Results From Carter and Stewart (1970) Experiments	61
Table 6.2 Elder and Tinkle (1980) Outdoor Burn Test # 4 Air Sampling Data	64
Table 6.3 Summary of Controlled Temperature Experiments by Elder and Tinkle (1980).....	66
Table A.1 Mechanical Properties of Pure Uranium Metal [Klein (1962)]	A-1
Table A.2 Selected Chemical Properties of Uranium Metal [Klein (1962)]	A-2
Table B.1 Excerpted Data from Table 1 of Baker et al. (1966).....	B-1

Acknowledgements

I would like to acknowledge the members of the Defense Nuclear Facilities Safety Board, Chief of Defense Nuclear Safety staff, Department of Energy employees, National Nuclear Security Administration personnel, especially the Y-12 National Security Complex staff for their patience and interest in expanding the depth of knowledge in this area. I would like to acknowledge the staff of the Oak Ridge National Laboratory Technical Research Library for their assistance in finding many of the reference documents in addition to many of the researchers and technical staff in Oak Ridge who provided documents and inputs from their own personal collections. I especially want to thank Jofu Mishima for the wealth of information he has personally provided and the time we spent together discussing release fractions, aerosols, and the oxide fume.

The cooperation and communication through the Department of Energy's Office of Science and Technical Information (OSTI), the Oak Ridge National Laboratory, the National Institute for Standards and Technology (NIST), and the International partners for Nuclear Information in Canada, England, France, Japan, and China has been invaluable in preparing this work.

Dedication

This work is dedicated to my wife Alicia “Lisi” and our three sons Daniel, Joshua, and James. Without their support this work would not have been possible given the numerous days spent at various research libraries in addition to the accumulation of numerous rare books for my own personal collection that spent many weeks cluttering up the dining room table. Thank you for your support as I travelled from location to location gathering information and preparing this work. Thank the Lord for travel mercies and the insight into this difficult subject, may the insights herein be used for your honor and glory. - Proverbs 3:6

Preface

Uranium is a rare earth metal of key importance in numerous industries. Uranium oxides have been used in numerous applications that can be traced back to the year 79 A.D. primarily as a glazing agent in pottery due to the spectral properties of each oxidation state. The discovery of the element is credited to Martin Heinrich Klaproth, a German chemist, in 1789, but uranium metal was not extracted until Eugène-Melchior Péligot first successfully reduced it in 1841 [Péligot (1842)]. Generally until the Manhattan Project began large-scale processing of uranium in the 1940's, there were very little inventories of uranium metal in existence. Since then the storage of large quantities of metal with significant oxidation potentials that can aerosolize under thermal stress (e.g. fire) has led to the evaluation of the risk these stores pose to the workers, members of the public, and the environment.

Uranium is a versatile element that can form numerous compounds, but the oxides are the forms that are most readily generated under thermal stress and also pose the largest health risk to human beings, primarily through inhalation. A general summary of uranium and the dry compounds (oxides and carbides) is provided discussing the different structures of each state. The reaction kinetics and selectivity as the oxidation progresses is discussed based on a specific area as applied to typical industrial metal forms at temperatures above and below the ignition point. Characteristics of potential fires are qualified for determining thermal stress. The creation of the oxide fume is outlined followed by dispersal characteristics of the aerosol. These molecular processes are related to the release fractions of uranium under fire scenarios which are compared with available experimental data from the regulatory handbook DOE-HDBK-3010 [DOE (1994)]. A critical look at the conclusions of the handbook and recommendations for revising the existing guidelines and for subsequent testing are made in the interest of ensuring that derived controls provide a commensurate level of protection appropriate for reducing the risk of accidents involving the oxidation of uranium metal.

This page intentionally left blank.

CHAPTER 1 - Uranium, the Element and Dry Compounds

Uranium is a naturally occurring element with numerous oxidation states, each having a variety of commercial applications that utilize the unique characteristics of each. Of primary interest is the metallic state which has commercial nuclear, industrial, and military applications. Uranium ore is normally processed using wet chemistry solutions and is reduced to metal form. Uranium metal has the highest density of the uranium forms and is stable under typical storage conditions. Additionally uranium metal can be alloyed with other elements to enhance various metallurgical properties of uranium for the intended application.

Depending on the isotopic enrichment of the uranium, the element can pose various radiological consequences, and depending on the oxidation state of uranium the compounds can pose various toxicological consequences. Uranium metal oxidizing in air can release an oxide fume that contains airborne particulate containing various uranium compounds. Exposure to the resultant aerosol can result in harm to workers, the general public, and the environment. The alloys of uranium metal can also enhance or reduce the various toxicological consequences through multiple methods under accident conditions.

Accordingly the response of uranium metal under fire conditions is of principal interest when attempting to predict the potential consequences of accidents involving uranium metal. This work outlines the progression of the oxidation of uranium metal with each of the stable oxide forms discussed in the following subsections. Selected thermodynamic properties and crystalline structure summary are provided at the end of the chapter for reference. Carbides are discussed since they are present in any cast uranium metal forms [Klein (1962)] and are part of the aerosol in the oxide fume. Additionally there are numerous other oxidation states and compounds of uranium that are possible in various solution media, but those compounds are omitted because they are not stable in the temperature range typically associated with a fire (e.g. 250 °C – 1000 °C). The response of uranium at reactor core temperatures and the effects of irradiated uranium are not discussed due to negligible differences in the kinetics with respect to irradiation and available literature supporting the nuclear power industry.

1.1. Uranium Metal (U)

Uranium metal has three primary metallurgic phases. The alpha (α), beta (β) and gamma (γ) phases exist at different temperatures in pure uranium, but each phase has different attributes that can be frozen using various trace elements in an alloy. These metallurgic phases each have a dramatic impact on how the metal oxidizes and each phase has a different affinity for production of the oxide fume. Also due to the heat transfer from the oxidation and heating of the metal during an accident, there are phase changes that need to be taken into account which impact the release of airborne particulate.

In pure form, uranium is a brilliant metallic white. Without any oxide, the metal has a mirror like quality reflecting light. Alloys are indistinguishable from pure metal unless $< 90\%$ uranium whereby the properties of the trace elements can be visible. The density and crystalline structure of the metal is dependent on the metallurgic phase which plays an important role in the generation of the oxide fume. The melting temperature of pure metal is $1080\text{ }^{\circ}\text{C}$, but trace contaminants from source materials or processing raise the melting temperature of most uranium materials into the $1100 - 1150\text{ }^{\circ}\text{C}$ range [Katz and Rabinowitch (1951)].

1.1.1 Alpha Phase

The α -phase is a ductile semi-plastic phase stable at temperatures up to $\sim 665\text{ }^{\circ}\text{C}$. The crystal structure of α -phase uranium is orthorhombic (space group V_h^{17}) as a distorted hexagonal closest packing [Katz and Rabinowitch (1951)]. This gives a density of 19.050 g/cm^3 for pure uranium at room temperature. This structure yields the semi-plastic nature of the α -phase demonstrating the anisotropy of the crystallographic direction [Katz and Rabinowitch (1951)]. The orientation of the crystal lattice determines the direction of thermal expansion, so wrought pieces will expand differently than cast pieces. Work hardening aligns the crystal structure within the α -phase as does annealing of cast pieces although the crystal orientation is different depending on the technique. This delays the allotropic transitions both on heating and cooling of the piece.

Uranium is in the α -phase under typical storage conditions. These properties are used in applications requiring semi-elastic response. The base state is prevalent in storage of ingots in metal processing facilities and where uranium is manufactured into other components.

1.1.2 Beta Phase

The β -phase is a brittle phase existing in the 665 – 775 °C range. The crystal structure of β -phase is difficult to determine because this structure cannot be frozen outside the temperature range without a trace element. Elements such as chromium, molybdenum, and titanium can be used to freeze the properties of the β -phase at ambient conditions. Indications from the chromium and molybdenum tests at less than 0.6% alloy are that the β -phase is orthorhombic with a larger crystal structure than the α -phase and lower symmetry. The nominal density of β -phase uranium is 18.97 g/cm³ based on measurements of the crystalline structure [Katz and Rabinowitch (1951)]. The larger, less symmetric crystals impart shear stress that lowers the bulk modulus of this phase leading to the brittle shedding of crystal layers. During the $\alpha \rightarrow \beta$ transition, the enthalpy change is 2.85 kJ/mol and the entropy change is 3.03 J/mol·K, while the heat capacity of the β -phase changes to 43.4 J/mol·K [Katz and Rabinowitch (1951)].

β -phase uranium is of interest in military applications, typically in depleted uranium armor penetrators. To freeze the properties of the β -phase, the typical alloy used is Staballoy, which is 0.75 – 3.5 % titanium depending on the exact munition specifications [Mishima et al (1985)]. The alloy must be quenched to maintain the properties of this phase (Harrington and Reuhle 1959). The brittle nature of the phase allows outer layers to shed as they oxidize to prevent slowing down the projectile and ensuring maximum translation of kinetic energy into the target. This phase is not expected to exist in non-military applications except as a transitional phase due to the thermal stress of processing or abnormal events.

1.1.3 Gamma Phase

The γ -phase shares many attributes with the ductile α -phase but exists in the 775 – 1050 °C range. The crystal structure of γ -phase uranium is body-centered cubic determined by high-temperature camera [Katz and Rabinowitch (1951)], and requires trace elements to freeze these phase properties at room temperature. The effects of the crystal structure reduce the density of γ -phase uranium to 18.89 g/cm³. Elements such as chromium, molybdenum, and niobium can be used to freeze the properties of the γ -phase [Katz and Rabinowitch (1951)]. The γ -phase is very plastic and bulk modulus is stronger than the α -phase due to the crystalline symmetry. This crystal lattice orientation shows uniform thermal expansion as opposed to the directional

indications of the α -phase. This leads to a more uniform phase with higher strengths which are the key desirable features of this phase. Uranium metal frozen in the γ -phase will not transition to the β -phase and retains the crystalline structure up to the melting temperature of the alloy which is higher than pure uranium, e.g. 1150 °C. During the $\beta \rightarrow \gamma$ transition, the enthalpy change is 4.78 kJ/mol and the entropy change is 4.52 J/mol·K, while the heat capacity of the γ -phase is 38.1 J/mol·K [Katz and Rabinowitch (1951)].

γ -phase uranium is of principal interest in the nuclear power industry where shapes need to be retained at higher temperatures for prolonged periods of time to ensure critical applications remain within their design tolerances. The niobium-uranium alloy at up to 6% niobium is the predominant material in this phase [Klein (1962)]. Quantities of this material are typically small due to the costs of processing material in this phase. The crystal grain structure of the alloy has to be homogenized to the greatest extent practical which is extremely labor intensive. The processing methods of metals with higher melting temperatures than uranium (e.g. niobium), require specialized equipment and the quenching of pieces to freeze this phase introduces many radiological concerns, including criticality, in and of itself when dealing with enriched uranium.

1.2. Uranium Monoxide (UO)

The first oxidation state for uranium is a single oxygen bond. The solubility of oxygen in uranium is small as is the solubility of uranium in uranium monoxide. Therefore the range of uranium to uranium monoxide is diphasic. The face-centered cubic crystalline structure has a rock salt structure with lattice constant $a_0 = 4.91 \text{ \AA}$ [Katz and Rabinowitch (1951)]. This structure is different than any of the three allotropic forms in the uranium metallurgical phases [Wilkinson (1962)]. These crystals are a mixed crystal that has been observed by x-ray evidence to show that the oxygen atom can replace carbon and nitrogen atoms present as contaminants in the metal. These crystals can also rearrange oxygen positions transporting disassociated cations through the metal matrix. However, UO has never been isolated in solid form at ambient conditions, thus no thermodynamic data exists for UO solids although observed in the crystal lattice. The patented process of forming a protective coat of UO on U metal provides the bulk of the available data [Watts and Cayless (1961)].

Uranium monoxide forms a protective coat insulating against thermal stress. Diffusion of oxygen into uranium at equilibrium can raise the melting point of the piece to 1133 °C. This process is relatively slow and virtually unstoppable at ambient conditions. This oxidation state as a solid protective coat in the treatment of uranium can stop oxidation at temperatures up to 600 °C [Watts and Cayless (1961)]. Incomplete coverage of the surface of uranium results in UO functioning as a nucleation point for the formation of higher oxidation states, whereby the transport of disassociated oxygen into the uranium increases leading to the formation of intermediate $UO_{1,x}$ compounds. Without treatment the UO layer is indistinguishable above ambient conditions.

1.3. Uranium Monoxide to Dioxide Intermediates ($UO_{1,x}$)

There are two predominant intermediates between UO and UO_2 , specifically U_3O_5 , and U_4O_7 . Each intermediate has been observed with a different crystalline structure. The diffusion of oxygen into uranium monoxide is faster once these intermediates are formed by UO nucleation. These oxides do not lose oxygen except at very high temperatures and low pressures. The crystalline structure for each oxide is different indicating that the formation is directly dependent on the orientation of the uranium monoxide lattice at the point of nucleation. U_4O_7 was identified first as a homogeneous face-centered cubic crystal [Katz and Rabinowitch (1951)]. This structure flows into the fluorite structures associated with uranium dioxide. U_3O_5 , a non-homogeneous face-centered cubic crystal, is also present as an intermediate between uranium monoxide and dioxide [Harrington and Reuhle (1959)].

Since these intermediates transition to other oxide states upon isolation, there is debate over whether or not they form stable states. Consensus is that the pair acts as a transport mechanism for oxygen through the oxide layer in a constant crystalline transformation process. U_4O_7 is predominant in the layer, such that these intermediates are commonly referred to as $UO_{1.75}$. These oxides are visible as a faint yellow progression through the color spectrum as the oxygen content of the outermost layer increases [Wilkinson (1962)]. This stage is very adherent and is difficult to separate from the uranium metal, ubiquitous with the U-UO system. The formation of $UO_{1,x}$ has been cited for preventing formation of a solid UO protective coat by expanding and bridging between nucleation points increasing oxygen diffusion into the uranium piece.

1.4. Uranium Dioxide (UO₂)

The first easily isolatable oxide state at ambient conditions is uranium dioxide. UO₂ is a very stable compound with melting temperatures up to 2760 °C [Belle (1961)]. Uranium dioxide has a face-centered cubic fluorite crystal structure (Figure 1.1) that allows for the transport of oxygen molecules [Katz and Rabinowitch (1951)]. Uranium dioxide in general application contains the pure dioxide and the intermediates between UO_{1.75} to UO_{2.33} since all have identical crystalline structure where the lattice constant decreases with increasing oxygen content. Therefore the density of UO₂ ranges from 9.75 to 11.08 g/cm³ with the density of pure UO₂ at 10.82 g/cm³ [Katz and Rabinowitch (1951)].

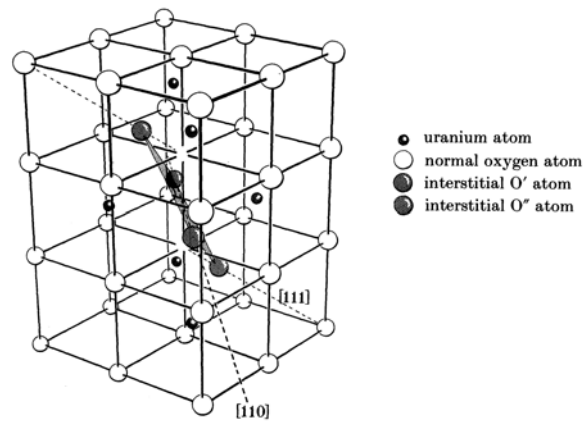


Figure 1.1 Face Centered Cubic Fluorite Structure of UO₂ [Allen and Tempest (1986)]

Uranium dioxide is one of the few compounds that is both ideally suited for high temperature nuclear reactor fuel and as a low temperature superconductor. The fact that the crystal lattice structure remains the same except for spacing over a wide temperature range and concentration gradient indicates the level of stability. The change in the structure is directly proportional to temperature and the flow of oxygen through the crystal lattice system. The visible color change of this reaction is a steel blue to purple to black transition on the uranium metal piece [Wilkinson (1962)]. The density fluctuations are fairly significant for the material itself and when compared to the 16 to 19.05 g/cm³ densities of uranium metal and the previous oxidation states, the UO₂ layer experiences a large volume expansion. The rate of this volumetric expansion determines the shear stress imparted on the underlying layer. The penetration of oxygen into UO₂ is surface limited to approximately 5 nm (50 Å) after which only disassociated oxygen atoms are available for further oxidation [McEachern and Taylor (1997)].

If the underlying layer is semi-plastic with a fair coefficient of thermal expansion like α -phase or γ -phase uranium, then the UO_2 layer will not separate from the metal at lower temperatures where the expansion coefficients are comparable, (e.g. $< 400\text{ }^\circ\text{C}$). However if the underlying layer is the brittle β -phase uranium or the temperature gradient is such that the stress exceeds the affinity of the layers, then the UO_2 may separate from the underlying layers [Harrington and Reuhle (1959)]. If separated from the bulk metal, the nucleation-and-growth mechanisms take over as the surface of the UO_2 is subject to oxidation quickly progressing the reaction to U_3O_8 at high temperatures. Notably as temperature increases, the size of the UO_2 particulate that will separate from a piece of uranium metal increases [Bennett and Price (1981)]. When separated as a particle, the entire UO_2 surface forms a 5 nm layer that diffusion limits further oxidation [McEachern and Taylor (1997)]. Therefore UO_2 is a nucleation point for particulate in the oxide fume and important constituent of the aerosol.

1.5. Uranium Dioxide to Triuranium Octaoxide Intermediates ($\text{UO}_{2,x}$)

There are three predominant intermediates between UO_2 and U_3O_8 . Each intermediate has been isolated as a stable form with a similar crystalline structure, identical except for the lattice spacing. The three intermediates are U_3O_7 , U_4O_9 and U_5O_{11} . As the oxygen to uranium ratio increases, the lattice distance decreases and the density of the particulate increases [Katz and Rabinowitch (1951)]. Each of these oxidation states has an alpha and beta phase crystalline structure. The alpha-phases are face-centered cubic and the beta phases are tetragonal. These phases have a crystallographic orientation preference dependent on the UO_2 or U_3O_8 lattice [McEachern and Taylor (1997)]. These oxidized states require a greater oxygen concentration gradient such that they are located on the exterior of the oxidizing layer, which given the density changes of the other oxide layers imparts more shear stress, especially as the crystalline phase change process occurs.

The impacts of the crystallographic orientation of $\text{UO}_{2,x}$ compounds are a compaction of the aerial density during phase transition and embrittlement of the oxide layer during interstitial oxygen transport. As the oxidation progresses the UO_2 sandwiched between the $\text{UO}_{1,x}$ and the $\text{UO}_{2,x}$ is expanding more rapidly than the outer layers of U_4O_9 and U_5O_{11} while the U_3O_7 is actually

expanding faster than the UO_2 [Katz and Rabinowitch (1951)]. The density progression during the transition from UO_2 to U_3O_8 is shown in Table 1.1. and Appendix A, Figure A.1. This leads to a cracking of the shell which fuels the oxide fume and creation of airborne particulate. The resultant micro-porosity in this layer further facilitates the diffusion of oxygen into the system progressing the reaction. Therefore if the shear stress imparted by the density fluctuations exceeds the bonding affinity of the lattice as it transports oxygen, then the layer will separate creating particulate that can be entrained if the aerodynamic equivalent diameter is sufficiently small (e.g. < 30 micrometers). When these density fluctuations are rapid at elevated temperatures, the layer appears to slough off in larger amounts as larger particulate [Coleman and Schwendiman (1962)].

Table 1.1 Selected Thermodynamic Properties of Uranium & Oxides (Grenthe et al, 2004)

	$\Delta_f G_m^0$	$\Delta_f H_m^0$	S_m^0	C_p^0	T_{melt}	ΔH_{fus}	T_{BP}	ΔH_{vap}	$p@ 1900 \text{ K}$	Density
	kJ/mol	kJ/mol	J/mol·K	J/mol·K	K	kJ/mol	K	kJ/mol	mm Hg	g/cm ³
$\alpha\text{-U}$	0	0	50.20	27.66	1353	9.14	4404	417.1	2.0×10^{-3}	19.05
UO_2	-1,031.	-1,085.0	77.03	63.60	3120	-	-	-	7.1×10^{-5}	10.97
$\alpha\text{-U}_4\text{O}_9$	-1,069.1	-1,128.0	83.53	73.34	-	-	**	**	**	11.18
$\beta\text{-U}_4\text{O}_9$	-1,069.1	-1,127.4	85.40	*	-	-	**	**	**	11.27
$\alpha\text{-U}_3\text{O}_7$	-1,080.6	-1,141.6	82.17	71.42	-	-	**	**	**	11.05
$\beta\text{-U}_3\text{O}_7$	-1,080.6	-1,142.0	83.51	71.84	-	-	**	**	**	11.36
U_3O_8	-1,123.2	-1,191.6	94.18	79.31	1403	-	**	**	**	8.39
$\beta\text{-UO}_3$	-1,123.2	-1,220.3	96.32	81.34	***	***	***	***	***	8.34
$\gamma\text{-UO}_3$	-1,123.2	-1,217.5	96.11	81.67	***	***	***	***	***	7.07

* $\beta\text{-U}_4\text{O}_9$ is not stable below 348 K, no C_p exists at reference temperature.

** Decomposes to UO_2 at temperatures above 1550 K.

*** Decomposes to U_3O_8 at temperatures above 1000 K.

Definition of Terms: $\Delta_f G_m^0$ standard molar Gibbs energy of formation,

$\Delta_f H_m^0$ standard molar enthalpy of formation

S_m^0 standard molar entropy

C_p^0 standard molar heat capacity

T_{melt} melting temperature

ΔH_{fus} molar heat of fusion

T_{BP} boiling temperature

ΔH_{vap} molar heat of vaporization

p vapor pressure at 1900 °K

1.6. Triuranium Octaoxide (U_3O_8)

This is the most stable form and predominant naturally occurring form of uranium oxide. This state is a dark olive-green-black compound that resists oxidation at ambient conditions. The natural ore pitchblende is a conglomeration of oxides ranging from UO_2 to U_3O_8 . When UO_2 and U_3O_8 are heated together, an orthorhombic needle shaped crystalline structure U_2O_5 can be formed that only exists when these compounds are mixed. As U_2O_5 uptakes oxygen during cation transfer, the crystalline form transitions to orthorhombic U_3O_8 without forming a new phase [Katz and Rabinowitch (1951)]. Therefore U_2O_5 is considered a homogeneous phase of the $UO_2 \cdot U_3O_8$ system. The orthorhombic form of U_3O_8 is shown in Figure 1.2 in comparison to the UO_2 lattice. U_2O_5 is an intermediate during the decomposition of U_3O_8 to UO_2 at temperatures above 1250 °C.

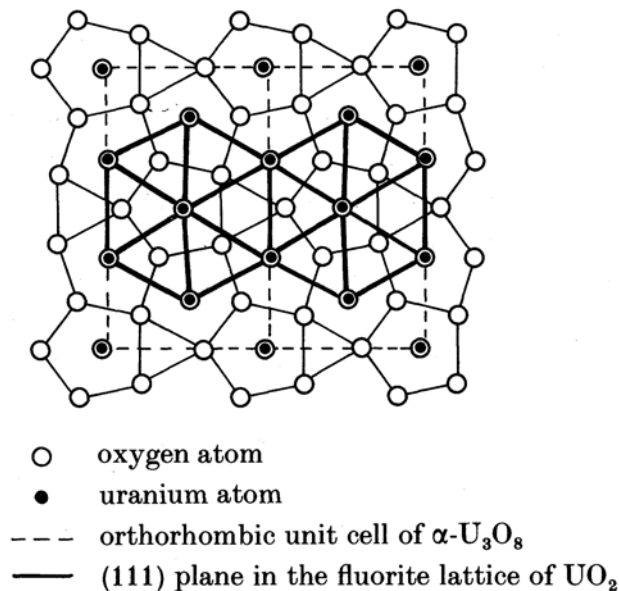


Figure 1.2 Comparison of Structures of UO_2 to U_3O_8 [Allen and Tempest (1986)]

As an oxide layer, the distinction can be made between the face-centered-cubic / tetragonal layers and the orthorhombic U_3O_8 layer. The porosity of the surface where U_3O_8 forms dictates if U_2O_5 will be produced or if the oxidation will more slowly progress to the U_3O_8 form. For most oxidations this is the final state reached under ambient conditions. The U_3O_8 lattice forms a hard coat on the material that is as dense as the surface structure will allow. U_3O_8 allows for the transfer of oxygen through the system to slowly oxidize underlying layers.

The density change to 8.39 g/cm^3 furthers the expansion of the U_3O_8 layer as U_3O_8 spreads across the rough surface formed with the other oxidation states and allowing direct contact between UO_2 and U_3O_8 . Depending on the surface roughness when this takes place, additional shear stress can be imparted that can displace relatively large chunks of oxide. Some of these pieces are visible slough which separates from the uranium piece exposing fresh material for oxidation, which based on the previous oxidation affinities is usually the $\text{UO}\cdot\text{UO}_{1,x}$ system. Chemical analysis of airborne particulate routinely indicates a large portion has progressed to U_3O_8 , but due to the reactions and the reliance upon the oxygen concentration gradients, the particulate may not necessarily be U_3O_8 at the point of generation. This oxidation state is the preferential end state for most natural reactions involving uranium.

1.7. Uranium Trioxide (UO_3)

Uranium trioxide can be produced via oxidation in two separate paths. The primary pathway is the oxidation of U_3O_8 through the normal progression of the reaction as the crystal lattice structure gradually transitions from orthorhombic U_3O_8 to hexagonal $\gamma\text{-UO}_3$. The crystal lattice transformation can be reversed and does reverse at temperatures above $750 \text{ }^\circ\text{C}$. This oxidation state has a dark yellowish-black visible appearance that was used to give Vaseline glass its unique appearance. The existence of this structure is made evident through the use of ultraviolet light refraction which enhances the distinct yellow qualities that are prevalent with this form of uranium oxide. A comparison between the structures of UO_2 and $\gamma\text{-UO}_3$ is shown in Figure 1.3.

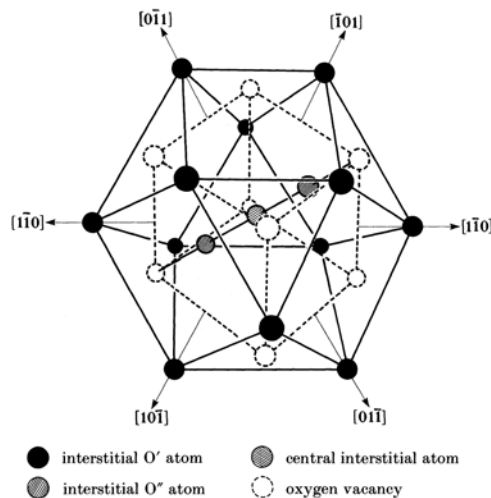


Figure 1.3 Comparison of Orthorhombic $\gamma\text{-UO}_3$ to Fluorite UO_2 [Allen and Tempest (1986)]

As a polymorphous compound, UO_3 has four distinct crystalline phases. The $\alpha\text{-UO}_3$ and $\beta\text{-UO}_3$ are formed by wet chemistry processes using strong acids and are not adherent out of solution. The $\delta\text{-UO}_3$ is a derivative of the face-centered fluorite structure of UO_2 and can be converted directly from UO_2 if the oxygen concentration gradient is sufficient or at high temperatures. At high temperatures the crystalline structure is difficult to stabilize given the polymorphous transition from $\delta\text{-UO}_3$ to $\gamma\text{-UO}_3$ the aforementioned decomposition of $\gamma\text{-UO}_3$ from the reverse reaction. The densities of each state are approximately 8.7 g/cm^3 indicating that UO_3 in either phase is more dense than the U_3O_8 compound but less dense than UO_2 in particulate form.

1.8. Uranium Carbides (UC_x)

Uranium carbides are highly stable uranium compounds with melting temperatures in excess of $2000 \text{ }^\circ\text{C}$. These compounds are routinely used in pebble bed nuclear reactors because of their bonding affinities [Klein (1962) and Schnizlein et al (1966)]. The crystalline structure is identical to uranium monoxide and the carbon can be transported the same as oxygen can [Stinton et al (1979) and Suzuki et al (1962)]. Table 1.2 summarizes the crystalline structures where comparison shows that UC_x has a compatible crystalline structure with UO , $\text{UO}_{1,x}$, and UO_2 . Uranium carbide is not formed from reaction with carbon dioxide or gases, but is actually a trace contaminant from the uranium processing [Harrington and Reuhle (1959) and Wilkinson (1962)]. The diffusion of uranium in graphite is quite large, but the diffusion of carbon into uranium is quite small as is the diffusion of oxygen in the $\text{U}\text{-}\text{UO}$ system [Katz and Rabinowitch (1951)]. Since graphite molds are the most economical for forming uranium metal pieces, the presence of uranium carbides is typically unintentional [Harrington and Reuhle (1959)].

Table 1.2 Summary of Crystalline Structures of Selected Uranium Compounds

	U	UO	$\text{UO}_{1,x}$	UO_2	$\text{UO}_{2,x}$	U_3O_8	UO_3
Orthorhombic	$\alpha \beta$					X	
Face-centered cubic		X	X	X	α		δ
Body-centered cubic	γ						
Tetragonal					β		
Hexagonal							γ

* Data is summarized from descriptions in Katz and Rabinowitch, 1951.

Uranium carbides are much harder than uranium oxides. The most prevalent carbides are uranium sesquicarbide (UC_4) and uranium monocarbide. Since carbon is transported like oxygen in the face-centered cubic lattice, the typical end state is uranium monocarbide. The concentration gradient for oxygen is much larger than that for carbon during the thermal oxidation of uranium metal, therefore the oxidation progresses more rapidly than the carbon can be transported to the interior of the system. As the oxidation progresses, the monocarbide is left as a sole segment with greater density than the layers expanding beneath it [Wakelin (1970)].

This inclusion cracks the oxide layers and is easily subjected to aerosol dispersal in the oxide fume [Stobbs and Whittle (1966)]. During oxidation of uranium metal where uranium carbides are present at the surface, the carbides will either be released as part of the aerosol or between slough layers of oxide that shed from the metal. Therefore in this process uranium carbides are treated as collateral damage and equivalent to uranium monoxide in final form and aerodynamic equivalent diameter properties.

CHAPTER 2 - Reaction Kinetics at Various Temperatures

On a microscopic level the oxidation reactions are progressing in one direction, from the surface of the material towards the interior. The transfer of oxygen and heat are predominantly in that direction. The oxygen concentration gradient is dependent on the concentration at the surface of the material and the heat transfer to support each reaction is dependent upon the mass of the material. Therefore to normalize the behavior and relate various shapes on a uniform basis, a surface area to mass ratio is necessary to quantify the driving kinetics of the reaction.

Uranium oxidation essentially occurs above or below the ignition point which can be translated to a temperature depending on surface area to mass ratio. Notably there is a transition region where the ignition of uranium cannot accurately be predicted. The selectivity of the progression and speed of progression of the oxidation through each of the oxidation states mentioned in Chapter 1 of this work are dependent on the ignition characteristics of the piece. The kinetics are discussed qualitatively and quantified based on empirical data.

2.1. Normalization and Use of Specific Area (cm^2/g)

Ignition temperature is defined as the temperature at which the oxidation reaction becomes self-sustaining. The ignition temperature of uranium metal is dependent on material size and shape. Studies on spherical powders demonstrate that uranium will ignite at temperatures as low as 250°C and that the ignition temperature is inversely proportional to the surface area [Coleman and Schwendiman (1962)]. Baker et al (1966) compiled data from ignition experiments on foil, wire and bulk samples, reporting ignition temperatures ranging from as low as 350°C for uranium foil (surface area = $49 \text{ cm}^2/\text{g}$) in air up to 700°C for single cubes (surface area = $0.38 \text{ cm}^2/\text{g}$). Ignition temperatures measured in air were slightly higher than those measured in pure oxygen. An abrupt transition is observed for surface areas in the vicinity of 2 and $5 \text{ cm}^2/\text{g}$ for pure oxygen and air, respectively [Baker et al (1966)]. Hence, a drastic drop in the ignition temperature is observed for uranium pieces that exhibit surface area values above this transition [Baker and Bingle (1966)]. This transition also corresponds to the point where forms may begin to exhibit pyrophoric properties.

2.1.1 Nominal Forms of Uranium Metal Storage

There are various nominal forms of bulk uranium metal storage depending on the intended application of the material. Industries that process large quantities of uranium (e.g. hundreds of kilograms or more) include the defense industry using the material for kinetic energy projectiles like armor penetrators and armor and the commercial nuclear fuel industry producing reactor foils. Facilities processing large quantities of uranium typically store the material as large billets or ingots.

These various applications are all slightly different depending on the unique characteristics of the end product, but a general overview of the simple geometry associated with three characteristic shapes and sizes follows. A range of values based on common configurations is used to characterize the traits of these shapes for how they will react under thermal stress.

2.1.1.1 Depleted Uranium Penetrators

Kinetic energy projectiles are essentially right cylinders with semi-tapered ends. These tapered ends are for aerodynamic stability, whereby the ends of most penetrators are blunt to ensure maximum translation of kinetic energy to the target. The lengths, diameters, and weights of these projectiles vary by the weapon for which they were designed. One of the most general use penetrators was the anti-tank XM774 which has been used in various experiments that are of direct interest for this work [Chambers et al (1982), Elder and Tinkle (1980), Glissmeyer and Mishima (1979), Hanson et al (1974), Jette et al (1989), and Mishima et al (1985)]. Therefore this work will use the XM774 simple geometry as the point of comparison.

The XM774 is a 34.5 cm long, 2.59 cm nominal diameter cylinder weighing 3355 ± 3 grams. Using simple geometry the nominal surface area of this shape is 291.25 cm^2 giving an average Specific area of $0.0868 \text{ cm}^2/\text{g}$. Other penetrators such as the M829A1 and XM900E1 penetrators have similar dimensions as shown in Table 2.1. These penetrators are typically a β -phase stabilized depleted uranium alloy, typically Staballoy with $< 1\%$ titanium [Jette et al (1990), Parkhurst et al (2004)]. The specific areas for these various penetrators are much smaller than the transition region and less than a quarter of the ratio where the ignition temperature exceeds $500 \text{ }^\circ\text{C}$.

Table 2.1 Specific Area for Depleted Uranium Penetrators

Designator	Diameter (cm)	Length (cm)	Surface Area (cm ²)	Mass (g)	Specific Area (cm ² /g)
M829A1	2.69	70.0	602.93	7343	0.0821
PGU-14/B	2.59	10.2	93.53	300	0.8205
XM774	2.59	34.5	291.25	3355	0.0868
XM900E1	2.03	76.2	492.43	4552	0.1082

* Data from Chambers et al (1982), Elder and Tinkle (1980), Glissmeyer and Mishima (1979), Hanson et al (1974), Jette et al (1989), and Mishima et al (1985).

2.1.1.2 Uranium Ingots and Billets

Uranium ingots and billets are stored in numerous shapes and sizes so that the material can easily be handled and/or worked into other products. Since uranium is expensive, the sizes of ingots and billets are typically suited to the intended application to minimize the waste material that must be recycled. Ingots typically weigh less than 20 kg so that an individual can physically move them. Machining stock for making penetrators or foils typically weighs less than 5 kg. These ingots are typically unit blocks so that stocks are standardized. Other dimensions are frequent when ingots are cut from larger billets or the process generates their own ingots for use as is common when materials are being alloyed.

Large billets designed to be moved by lift truck are typically limited to a metric ton to assist inventory and simplify storage. These billets are usually a nominal 1x2x3 unit block designed to fit on a pallet. The weight of an ingot or billet depends on the alloy of the material. For this study, the nominal density of uranium alloy, 18.9 g/cm³, is used to determine the mass of the shape. A variety of different sizes and masses are shown in Table 2.2.

Table 2.2 Specific Area for Typical Uranium Ingots and Billets

Unit Block	Length (cm)	Width (cm)	Height (cm)	SA (cm ²)	Mass (g)	cm ² /g Ratio
1 x 2 x 2	5.08	5.08	2.54	103.23	1,239	0.0833
1 x 2 x 3	61.98	41.32	20.66	9390.33	1,000,000	0.0094
1 x 3 x 5	12.70	7.62	2.54	296.77	4,646	0.0639
1 x 5 x 7	17.78	12.70	2.54	606.45	10,840	0.0559
2 x 3 x 4	10.16	7.62	5.08	335.48	7,433	0.0451

2.1.1.3 Reactor Foils

Reactor foils are unique to each reactor design. The latest trend has been a shift away from solid uranium metal foils to other designs. Many of the reactor foils in newer designs are uranium oxide sandwiched between aluminum sheets such that during accident conditions the aluminum melts away allowing the fuel to fall out of critical geometry [Klein (1962)]. However many research and high performance reactors still use solid uranium metal foils or have the capability to use that fuel such that nuclear industry processes these shapes [Klein (1962)]. Reactor designs that use pebble beds are not discussed since the majority of the designs use uranium carbide pebbles as opposed to uranium metal which was chosen because uranium carbide does not oxidize as readily. Reactor foils of solid uranium are rolled and formed from ingots of uranium metal at processing plants throughout the world [Harrington and Reuhle (1959)].

Reactor foils that have utilize solid uranium metal typically use a parabolic thin sheet with dimensions ranging from 1/8th inch (3.2 mm) to 1/64th inch (0.4 mm) thick with foils ranging from 100 cm² to 1 m² [Megaw et al (1961) and Klein (1962)]. The mixing of the units on these specifications indicates that the machining was performed in either the United States or United Kingdom where machining thicknesses have been calibrated to the Imperial System. Nonetheless, these nominal dimensions have large specific areas ranging between 1 cm²/g and 9 cm²/g. This large surface area also leads to quick oxidation of the metal under air storage, such that the foils are designed to be in aqueous solution. Many of these foils are immediately submerged in a fluid after final dimensional inspection to minimize oxidation.

2.1.2 Nominal Forms of Uranium Metal Byproducts

As uranium metal is processed from ingots and cast shapes into final forms, there are a variety of byproducts. When saws are used to cut through material, small fines are generated depending on the properties of the teeth on the cutting edge. For hard metals such as uranium, these saw fines are usually weighed on the milligram level [Harrington and Reuhle (1959)] with specific areas > 1000 cm²/g. The friction of the cutting process generates large amounts of heat such that either the process is done under an aqueous coolant or the fines oxidize immediately upon generation. Saw fines are pyrophoric when exposed to oxygen, but with little mass they are typically not present in large quantities [Coleman and Schwendiman (1962)].

A more significant byproduct of metal processing is chips and turnings from the machining processes. Turnings are typically generated on a lathe or mill where the properties of the turning are depending on the cutting edge, the depth of the cut, and the material. Chips are generated under other typical metalworking activities and are usually intermixed with turnings for reprocessing and recovery of the uranium. The generation of chips and turnings is typically done under a coolant due to the heat of friction associated with the cuts, however chips and especially turnings have enough mass and rigidity to either fall out of the coolant or accumulate such that portions are not submerged exposing them to oxygen [Harrington and Reuhle (1959)].

Chips and turnings have specific areas similar to reactor foils ranging from 2 cm²/g to 10 cm²/g. Chips with ratios of 9 cm²/g are typically readily available for testing and performing experiments. At this size these byproducts are extremely pyrophoric in air, therefore most processing facilities briquette their chips and turnings into compressed ingots minimizing the surface area [Wilkinson (1962)]. These briquettes are then melted down during the next casting cycle and returned to either a shape or ingot for storage or sent to some other recovery system. The quantity of chips and turnings is directly proportional to the throughput of the facility and is of paramount concern due to the pyrophoric nature of the materials. In the case of some penetrators as much as 70% of the ingot is turned to chips and turnings during the production of the piece [Harrington and Reuhle (1959)]. Uranium byproducts will be assumed to have specific areas greater than 2 cm²/g.

2.2. Uranium Oxidation

Uranium oxidation progresses in the presence of oxygen, regardless of temperature. As temperature increases the oxidation reaction can become self-sustaining at the point of ignition. The relationship between the ignition temperature and the specific area is shown in Figure 2.1 supported in Appendix B. There are various points in this curve that indicate that in many of the uranium forms discussed above, ignition is not a possibility [Baker et al (1966)]. Subsequently the general treatment of the oxidation progression applicable to the bulk forms discussed in the previous section are handled qualitatively using the data characteristics presented in Chapter 1 as oxidation at temperatures below the ignition temperature.

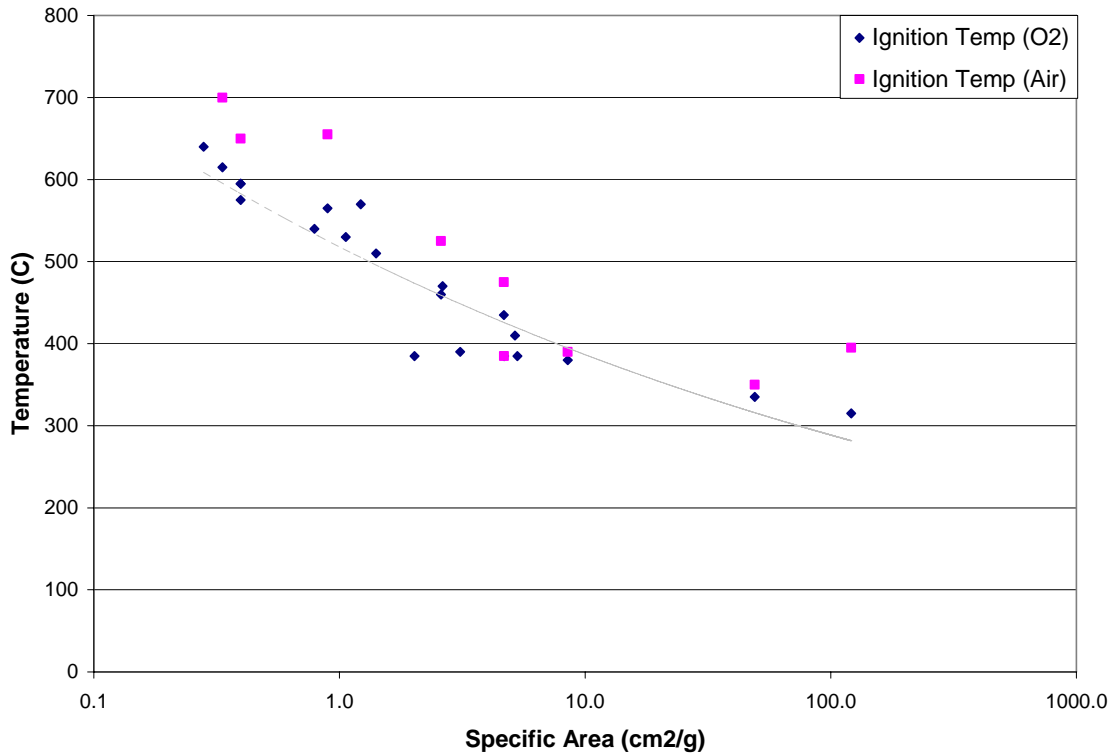


Figure 2.1 Relationship Between Specific Area and Uranium Ignition. [Baker et al (1966)]

2.2.1 Oxidation Below the Ignition Temperature

At temperatures below the ignition temperature the reactions are not self sustaining and extinguish upon loss of external heat source [Baker et al (1966), Coleman and Scwendiman (1962), Elder and Tinkle (1980), Hilliard (1958), Katz and Rabinowitch (1951), and Megaw et al (1961)]. Therefore the speed and progression of the oxidation is directly proportional to temperature. At low temperatures the reaction kinetics of the initial reactions are parabolic, and in general asymptotic, linear at higher temperatures indicating non-ignition reactions are dominated by oxygen diffusion [Baker and Bingle (1966), Bennett and Price (1981), Cubicciotti (1952), Gittus (1963), Guéneau et al (2002), Hilliard (1958), Isaacs and Wanklyn (1960), Leibowitz et al (1961), Megaw et al (1961), Pizzolato et al (1957), and Schnizlein et al (1959)].

Uranium metal immediately upon machining has a pure uranium surface layer that is slowly oxidized under ambient conditions. The unoxidized base state is depicted in Figure 2.2 as a reference point for further oxidation. The first oxidation occurs as the hexagonal lattice reorients to a face-centered cubic by disassociating the oxygen molecules. The resultant state is a very

adherent layer of cubic crystals attached to hexagonal structure forming a skin on the material [Katz and Rabinowitch (1951)]. This state is depicted in Figure 2.3 although this layer is not continuous unless uranium treatment has been performed [Watts and Cayless (1961)]. Since the diffusion is very slow the oxygen atoms at this point are oriented away from the majority of the uranium metal [Bloch et al (1982) and Colmenares et al (1981)]. The change in enthalpy results in a heat of formation of UO from U of 575 kJ/mol [Katz and Rabinowitch (1951)] releasing a large amount of energy.

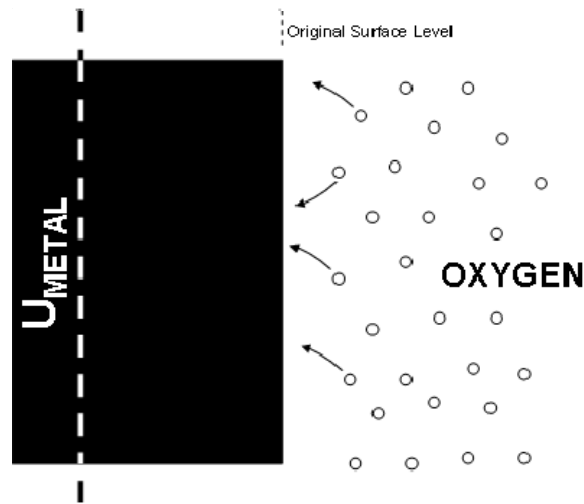


Figure 2.2 Unoxidized Uranium Reference Diagram.

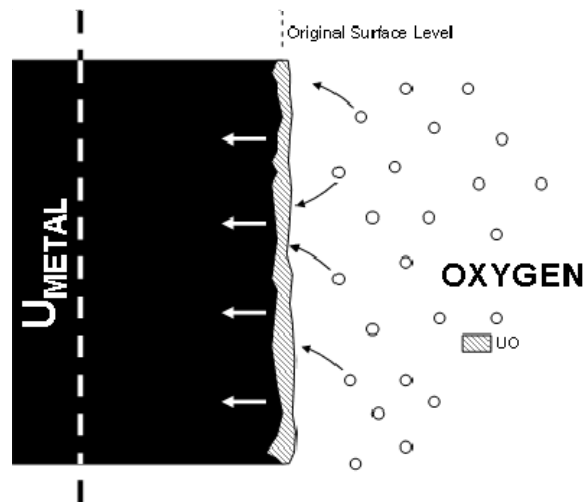


Figure 2.3 Uranium Monoxide Layer Formation.

The face-centered cubic lattice translates oxygen from the surface to the interior to oxidize the uranium metal allowing the cubic lattice to accept more oxygen and form $UO_{1,x}$ compounds. The parabolic kinetics in the less than 190 °C range are demonstrated through slow progression of these oxide layers at ambient conditions, but almost instantaneous translation through these states at temperatures above 100 °C. As this reaction accelerates, more energy is released raising the local temperature to the range where uranium dioxide can be formed, but at lower temperatures the reaction is slow enough for the uranium metal to act as a heat sink and keep the reaction on the slow portion of the curve [Bennett and Price (1981)]. The amount of energy released as uranium metal transitions to UO_2 is 1085 kJ/mol as shown in Table 2.3 ($\Delta_f H_m^0$), indicating that approximately half the energy is for to the U to UO conversion and half for the UO to UO_2 reaction. When compared to a nominal heat capacity of uranium at 27.66 J/mol.K and uranium dioxide at 63.6 J/mol.K these energies can quickly accelerate the local reaction.

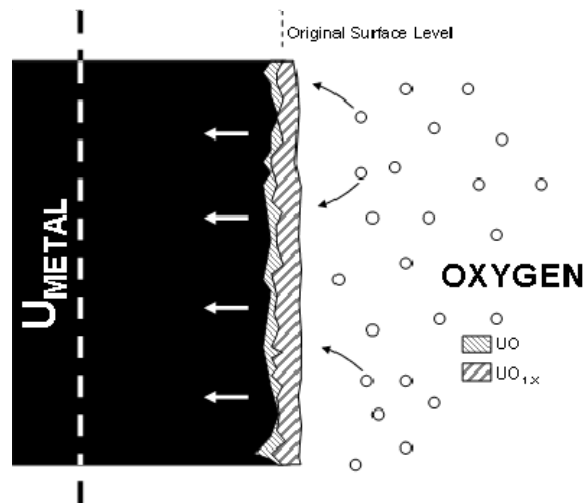


Figure 2.4 Uranium Skin Formation.

Either after a long duration or at high temperatures, the $UO_{1,x}$ compounds begin to nucleate the formation of UO_2 . The subsequent density change is a significant expansion as shown in Table 2.3. The next oxidation layer begins to expand significantly with the expansion directly linked to the local temperature and speed of the reaction. The surface roughness increases significantly and the shear stress imparted by this expansion can cause the oxide layer to slough from the surface of the metal [Bloch et al (1982)]. The increase in the thermal resistivity, demonstrated by the changes in heat capacity as shown in Table 2.4 for the oxide layers insulates the uranium.

At low temperatures with slow kinetics, this reaction can eventually consume all of the material without translating to higher oxidation states [Coleman and Schwendiman (1962)]. If the oxidation of uranium completely takes place with temperatures never exceeding 190 °C, then uranium dioxide will be the final state [Leibowitz et al (1961)]. If the reaction occurs in the 190 °C to 225 °C, then there is sufficient energy to continue on to other oxidation states. At higher temperatures the oxide layer more readily separates from the metal exposing lower oxidation states to both higher temperatures and a higher oxygen concentration [Pizzolato et al (1957)]. The volumetric expansion and roughness of the UO_2 layer is depicted in an adherent state in Figure 2.5. A spectral microscopic image of the surface roughness in an adherent UO_2 state is shown in Figure 2.6.

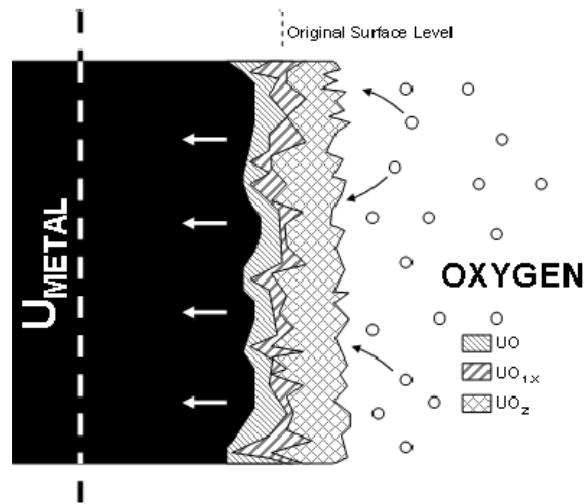


Figure 2.5 UO_2 Layers and Surface Roughness.

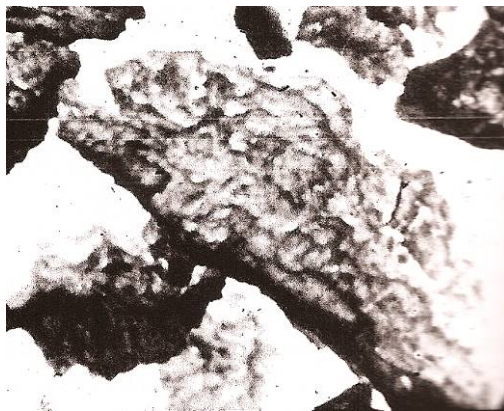


Figure 2.6 UO_2 Surface Image [Mishima et al (1985)]

In the adherent state where the oxide does not separate from the metal, the oxidation progresses to uranium dioxide intermediates $\text{UO}_{2.x}$. This reaction only occurs at temperatures in excess of $190\text{ }^\circ\text{C}$ but is variable such that the localized temperature from the exothermic oxidation of uranium or thermal stress from an outside source can create these compounds [Bennett and Price (1981), Gittus (1963), and Katz and Rabinowitch (1951)]. With allotropic lattice structures, similar to both the UO_2 and U_3O_8 structures, $\text{UO}_{2.x}$ acts as interstitial glue between the different crystalline structures [Leibowitz et al (1961)]. The kinetics of this transformation is parabolic in nature indicating the change of the lattice structure [Aronson et al (1957)]. An Arrhenius plot for the formation of U_3O_7 on UO_2 is shown below as Figure 2.7 [McEachern and Taylor (1997)].

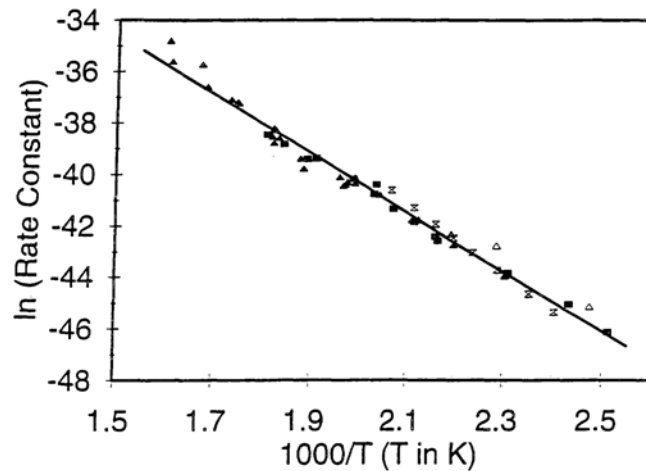


Figure 2.7 Arrhenius Plot for $\text{UO}_{2.x}$ Formation on UO_2 [McEachern and Taylor (1997)]

The $\text{UO}_{2.x}$ compounds have densities less than the oxidation states on either end, such that if the outermost layer is the $\text{UO}_{2.x}$ and there is insufficient kinetic energy to progress to U_3O_8 , then the layer will expand and float on UO_2 like a skull layer on molten metal. This exposes voids and creates cracks in the $\text{UO}_{2.x}$ layer that further increases the surface roughness [Isaacs and Wanklyn (1960) and Stobbs and Whittle (1966)]. The increase in the surface roughness coupled with the shear stress from the faster expanding underlying UO_2 layer makes this oxidation state prone to separation. Local micro-turbulence in the layer defects assists aerosolization and oxygen transport into the material increasing volumetric expansion induced surface roughness [DOE (1976)]. The effects of this process are shown in Figure 2.8. The surface roughness of this state has been captured by spectral microscopy as shown in Figure 2.9.

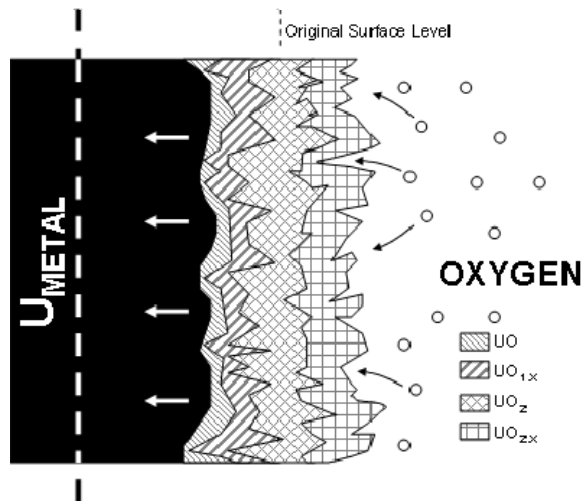


Figure 2.8 Uranium Dioxide Intermediates

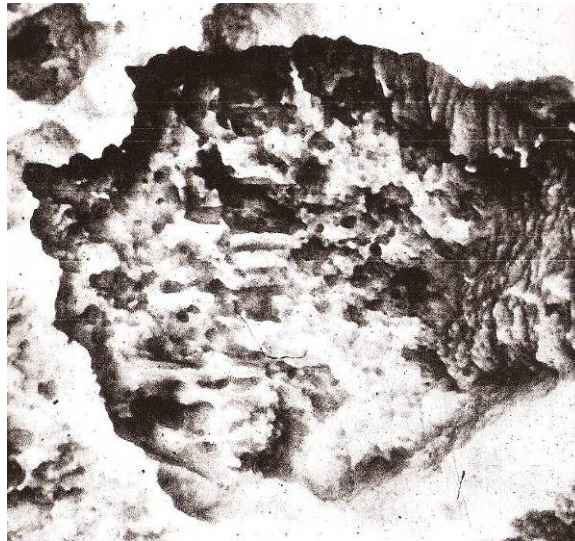


Figure 2.9 UO_{2,x} Surface Image [Mishima et al (1985)]

The relative end state of most thermal stress reactions is the oxidation of $\text{UO}_{2,x}$ into U_3O_8 . At temperatures in excess of $350\text{ }^\circ\text{C}$, U_3O_8 is the only end state observed [Baker and Bingle (1966), Coleman and Schwendiman (1962), Hilliard (1958), and Peakhill and Antill (1960)]. The U_3O_8 expansion introduces additional stress on the material. The thermal stress from the oxidation is coupled with a volumetric expansion significantly greater than UO_2 with a different crystal structure. The surface cracks in the underlying layer expand significantly and fissures accelerate the oxidation [Isaacs and Wanklyn (1960) and Stobbs and Whittle (1966)]. This reaction is not observed at temperatures less than $190\text{ }^\circ\text{C}$ indicative of the activation energy required.

The reaction progresses in a manner that introduces volumetric expansion in the UO_2 and U_3O_8 layers compressing the $\text{UO}_{2,x}$ intermediates allowing for direct UO_2 and U_3O_8 communication. Since the $\text{UO}_{2,x}$ layer functions as a binding medium between the two, when directly in contact the lattice structure differences introduce void spaces that facilitate the shedding of the U_3O_8 layers. If the reaction progresses slowly, then the $\text{UO}_{2,x}$ intermediates will have a time to form and the layers will not separate as indicated in Figure 2.10. This can lead to some significant protrusions of U_3O_8 from the surface leading to the surface roughness shown in Figure 2.11.

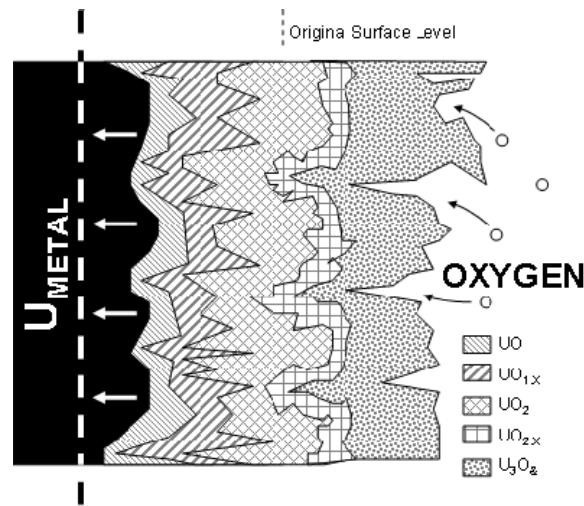


Figure 2.10 Formation of the U_3O_8 Oxide Layer.

These reactions apply to the penetrators, ingots, and billets as indicated in section 1 of this chapter since there have been no observable ignition temperatures beneath the melting point for these surface-area-to-mass ratios. Over 110 years of study on this oxidation reaction has led to the development of a Gibbs-free energy determination model to predict the portion of uranium in each oxidation state as a function of temperature [Guéneau et al (2002)]. These models are used to calculate standard enthalpy, entropy, and heat capacity of the mixture as shown in Table 2.3 and to confirm the heat capacities shown in Table 2.4 [Grenthe et al (2004)]. The agreement between the calculated data and experimental results between 1947 and 1993 are well within the margin for instrument error in the experiment. The asymptotic nature and parabolic portions of the curves have been demonstrated using the Gibbs free energy model allowing the generation of phase diagrams for these materials under various thermal stress as shown in Figure 2.12 [Guéneau et al (2002)].

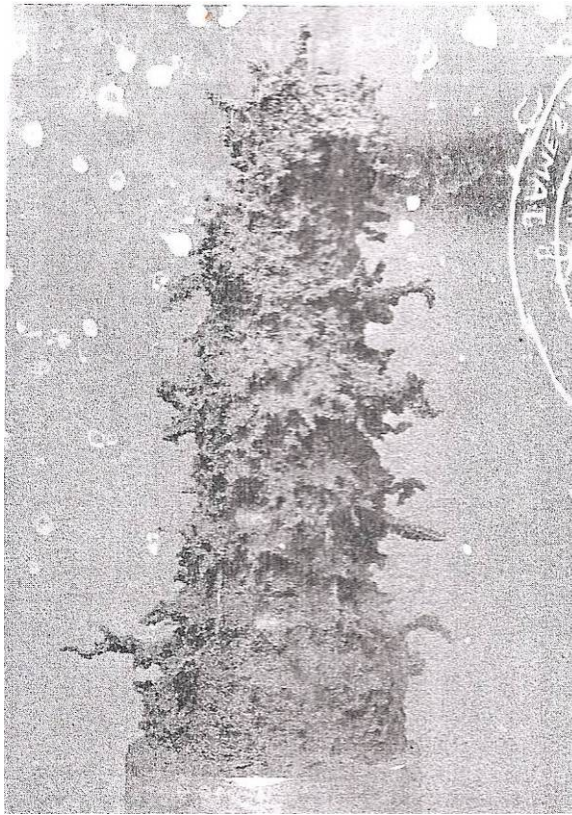


Figure 2.11 U_3O_8 Surface Image [Megaw et al (1961)]

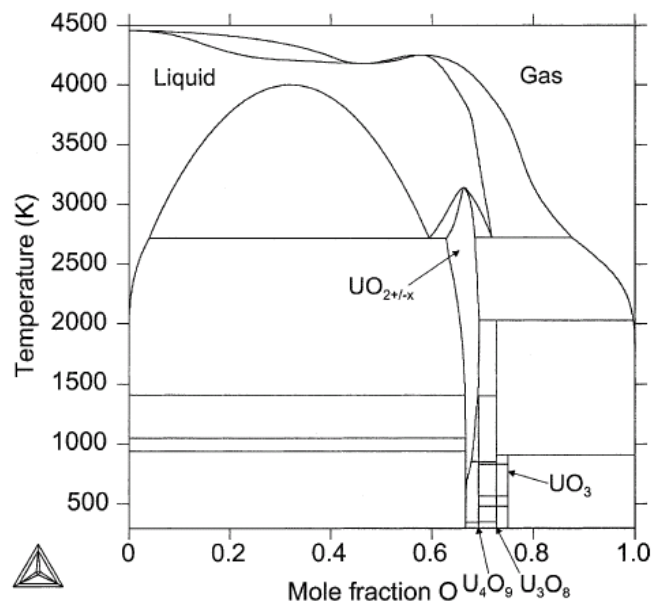


Figure 2.12 Phase Diagram for U-O at 1 Bar [Guéneau et al (2002)].

Table 2.3 Selected Thermodynamic Data of Uranium & Oxides at 298.15 K

	$\Delta_f G_m^0$	$\Delta_f H_m^0$	S_m^0	$C_p^0_m$	Density
	<i>kJ/mol</i>	<i>kJ/mol</i>	<i>J/mol·K</i>	<i>J/mol·K</i>	<i>g/cm³</i>
α -U	0	0	50.20 ± 0.20	27.66 ± 0.05	19.05 ± 0.05
UO ₂	-1,031.8 ± 1.0	-1,085.0 ± 1.0	77.03 ± 0.20	63.60 ± 0.08	10.97 ± 0.15
α -U ₄ O ₉	-1,069.1 ± 1.7	-1,128.0 ± 1.7	83.53 ± 0.17	73.34 ± 0.15	11.18 ± 0.1
β -U ₄ O ₉	-1,069.1 ± 1.7	-1,127.4 ± 1.7	85.40 ± 0.20	*	11.27 ± 0.2
α -U ₃ O ₇	-1,080.6 ± 1.4	-1,141.6 ± 1.4	82.17 ± 0.50	71.42 ± 0.30	11.05 ± 0.1
β -U ₃ O ₇	-1,080.6 ± 1.4	-1,142.0 ± 1.4	83.51 ± 0.20	71.84 ± 0.14	11.36 ± 0.3
U ₃ O ₈	-1,123.2 ± 0.8	-1,191.6 ± 0.8	94.18 ± 0.17	79.31 ± 0.16	8.39 ± 0.5
β -UO ₃	-1,123.2 ± 0.8	-1,220.3 ± 1.3	96.32 ± 0.40	81.34 ± 0.16	8.34 ± 0.7
γ -UO ₃	-1,123.2 ± 0.8	-1,217.5 ± 3.0	96.11 ± 0.40	81.67 ± 0.16	7.07 ± 1.0

* β -U₄O₉ is not stable below 348 K, no Cp exists at reference temperature.

The standard molar energies of formation are: Gibbs ($\Delta_f G_m^0$), Enthalpy ($\Delta_f H_m^0$), Entropy (S_m^0) and Heat Capacity ($C_p^0_m$) [DATA ranges from Katz and Rabinowitch (1951), Glassner (1957), Grenthe et al (2004), and Guéneau et al (2002)]

Table 2.4 Heat Capacities of Uranium Oxides [Grenthe et al (2004)]

	T _{min} (K)	T _{max} (K)	a	b	c	e
UO ₂	250	600	62.774	31.74		
α -U ₄ O ₉	250	348	1487.6	-6973.7	9.736	-178.6
β -U ₄ O ₉	348	600	79.089	13.65		-10.38
α -U ₃ O ₇	237	347	64.149	49.14		-6.72
β -U ₃ O ₇	232	346	64.338	49.79		-6.55
U ₃ O ₈	233	600	87.276	22.46		-12.44
β -UO ₃	298	678	86.170	24.98		-10.915
γ -UO ₃	298	850	88.103	16.64		-10.128
UO ₃	400	650	76.010	38.06		-2.31

$$C_p \text{ (J/mol}\cdot\text{K)} = a + 10^{-3}bT + 10^{-3}cT^2 + 10^5eT^{-2}$$

2.2.2 Oxidation Above the Ignition Temperature

Oxidation above the ignition temperature is not dominated by diffusion; instead the uranium directly oxidizes without relying upon diffusion or the crystalline transport of disassociated cations. Above the ignition temperature the reactions proceed very quickly from uranium metal to U_3O_8 and the volumetric expansions and contractions with local temperature fluctuations help to slough off the oxide coat and expose more material for direct oxidation [Baker and Bingle (1966), Bennett and Price (1981), Cubicciotti (1952), and Gittus (1963)]. Since there is no delay in disassociating the oxygen for diffusion these reactions release more energy rapidly elevating local temperatures as shown in Figure 2.13. The resultant 1191.6 kJ/mol is released at a much faster rate than the slow progression through the crystalline transformation facilitating acceleration of the reaction. The adiabatic flame temperature of this oxidation is 2000 °C, indicating that the maximum burning temperature observed after ignition is 85% of the theoretical maximum.

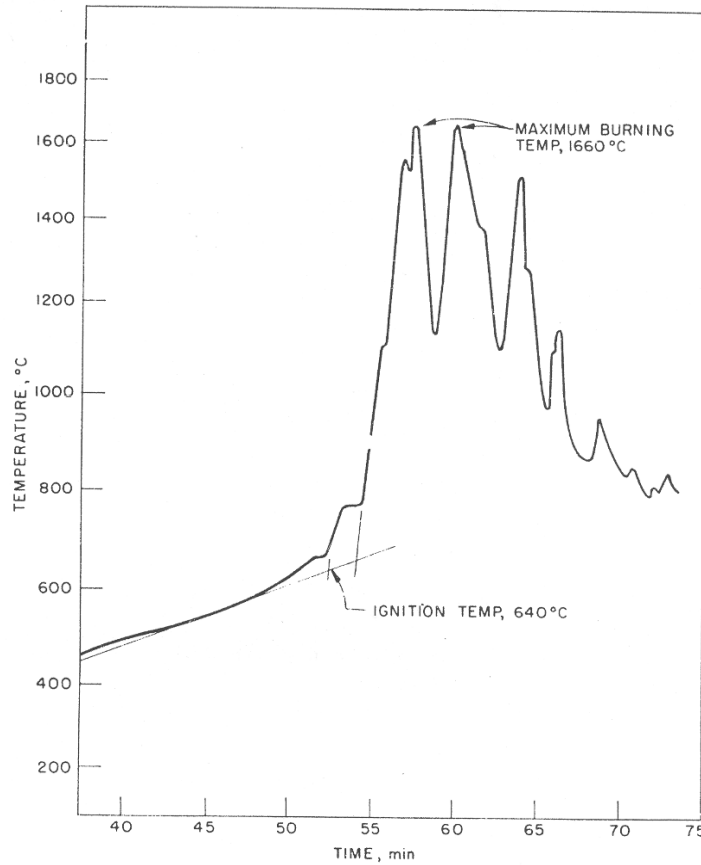


Figure 2.13 Temperature Profile After Uranium Ignition [Baker et al (1966)]

Reactions above the ignition temperature generate more airborne particulate as the available uranium oxidizes and does not have time to form large stable crystalline structures or absorb heat into the material [Peakhill and Antill (1960) and Schnizlein et al (1959)]. These reactions behave according to straight-line Arrhenius laws [Baker and Bingle (1966) and Katz and Rabinowitch (1951)] with activation energy of 102 kJ/mol [Aronson et al (1957)]. When compared to the 154 kJ/mol activation energy for diffusion controlled oxidation [McEachern and Taylor (1997)], the oxidation reactions occur more easily once the ignition temperature has been reached. There appears to be no selectivity between UO_2 and U_3O_8 after ignition and intermediate compounds have not been isolated. Available data compare these oxides to the high temperature oxides that are exclusively U_3O_8 when the residue was being dissolved for delayed neutron interrogation [Aronson et al (1957) and Baker and Bingle (1966)]. The comparison between a piece of uranium oxidized above and below the ignition temperature is shown in Figure 2.14.

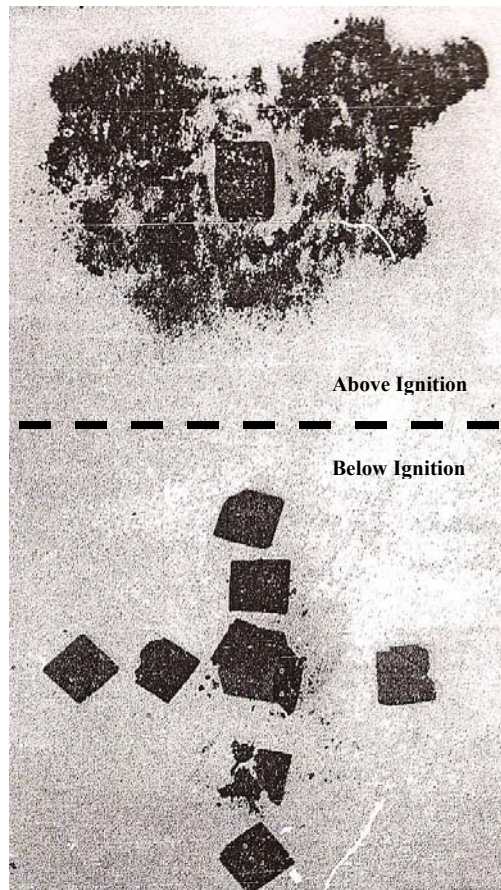


Figure 2.14 Uranium Oxidation Above & Below Ignition Temp [Baker and Bingle (1966)]

The fast oxidation of uranium after ignition elevates local temperatures past the melting point of uranium which fosters the formation of small particulates [Baker et al (1966)]. The higher localized temperatures at the oxidizing surface are above the melting point of U_3O_8 and are self limited by the decomposition of U_3O_8 to UO_2 at high temperatures. The rapid density change from metal at 19 g/cm^3 to U_3O_8 at 8.4 g/cm^3 combined with the potential liquefaction of microdroplets on the oxidizing surface combine to form the finely divided oxide evident in Figure 2.14. Combined with the absence of the adherent intermediate $UO_{2,x}$ states and the crystalline structure incompatibilities, the oxide generated upon the ignition of uranium is a fine ash. The particulate size distribution from sieve analysis of the resultant oxide [Mishima et al (1985)] demonstrates the preference for smaller particulate generation as shown in Figure 2.15. Therefore uranium oxidizing above the ignition temperature will generate more airborne particulate than uranium oxidizing below the ignition temperature due to the creation of smaller particulate which can be more easily entrained in the oxide fume.

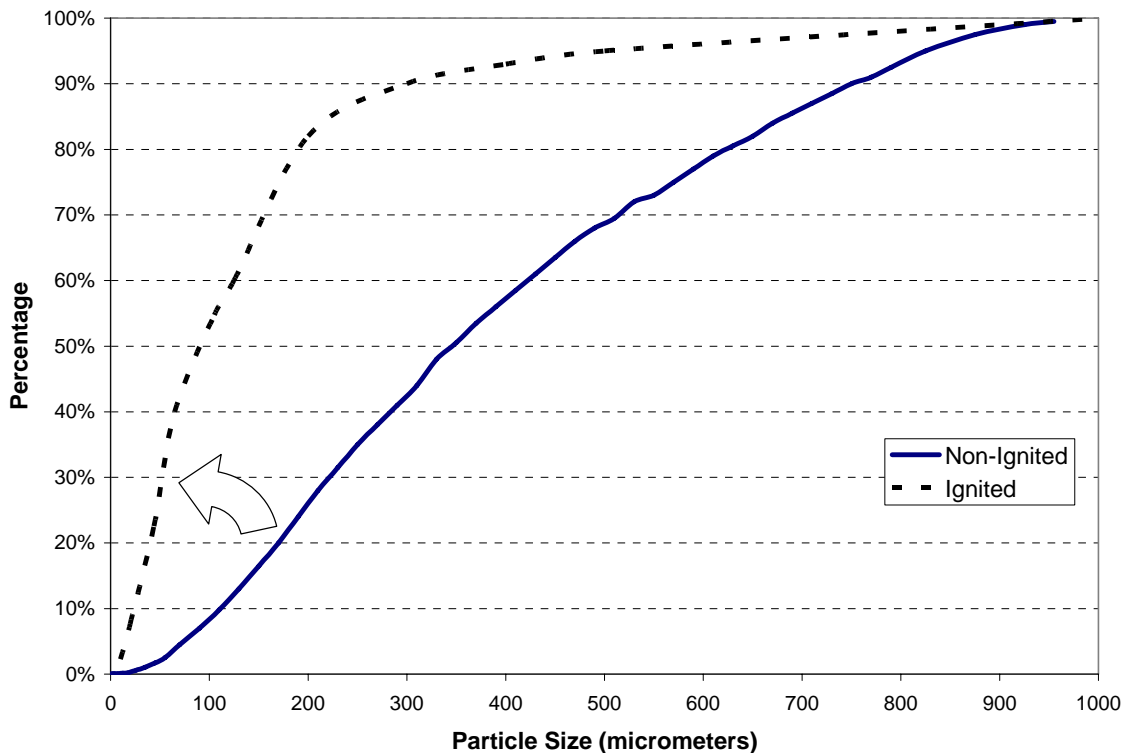


Figure 2.15 Cumulative Distribution of Particulate Size Above & Below Ignition (Baker et al, 1966)

2.2.3 Oxidation in the Transition Region

Oxidation in the transition region is complicated by the competition for direct oxidation and the diffusion of oxygen into the system. Crystalline structure orientation and the elasticity of the uranium metal can slow the sloughing of oxide layers which changes the response of the material. Looking at the experiments of Baker et al (1966), the sample media were exclusively α -phase uranium with negligible trace elements cut into the desired size. The difference in the ignition temperatures recorded could be due to surface defects which selectively enhance direct oxidation compared to diffusion. The energy balance used to predict ignition temperature is shown below as Equation 1 which outlines the balance between the heat generation and heat loss.

Equation 1 Energy Balance for Uranium Ignition [Baker et al (1966)]

$$C_p \frac{\partial T}{\partial t} = \frac{QM_U S}{10^3 M_{O_2}} \frac{\partial w}{\partial t} - hS(T - T_a) - \sigma \epsilon S(T^4 - T_a^4)$$

Generation Convection Radiation

Where: C_p is the specific heat of uranium (0.044 cal/g · °K)
 T is the metal temperature (°K)
 T_a is the ambient air temperature (°K)
 t is time (min)
 Q is the heat of reaction (1089 cal/g U)
 M_u is the molecular weight of uranium (238 g/mol)
 M_{O_2} is the molecular weight of oxygen (32 g/mol)
 S is the Specific Area (cm²/g)
 w is the quantity of oxygen reacted (mg/cm²)
 h is the heat transfer coefficient (0.03 cal/cm² · °K · min)
 σ is the Stefan-Boltzman constant (81.6 x 10⁻¹² cal/cm² · min · °K⁴)
 ϵ is the total emissivity of the oxidized surface (0.75)

Available data indicate that oxygen lowers the ignition temperature compared to air as shown in Figure 2.1. Currently no models have been developed for the transition region which has been observed at specific areas as low as 1.6 cm²/g and as high as 6 cm²/g. The main breakdown of the model is the radiant heat loss is highly dependent on the localized temperature which fluctuates significantly and there is no account for radiant heating of the oxidizing piece onset by nearby radiant bodies. When combined with the variations in local specific area as parts of the piece oxidize, the energy balance becomes much more difficult to close especially as oxygen depletion accelerates and decomposition occurs.

The general differential form of the rate equation has been determined by empirical fit as shown in Equation 2 [Baker et al (1966)]. Given the complexity of the transition region the application in general industry is to use a straight line approximation for estimating the ignition temperature. Materials with specific areas greater than 1 cm²/g are typically assigned an ignition temperature of 400 °C. However, the instabilities in energy balance closure are typically manifested visually as pyrophoric properties. Localized temperature increase leading to ignition of the piece in the transition region are associated with the general determination that uranium materials with specific areas greater than 1 cm²/g are pyrophoric.

Equation 2 Differential Form of the Rate Equation for Equation 1

$$\frac{\partial w}{\partial t} = \frac{5}{6} w^{-1/5} 1.8 \times 10^4 \exp\left[-\frac{14300}{RT}\right]$$

Observations have been made that in the transition region the presence of uranium carbide as an inclusion can cause the oxide surface to crack inducing separation of the oxide layers and exposing lower oxidation states to direct oxidation at elevated surface temperatures. The progression of this oxide cracking is shown below in Figures 2.16 and 2.17 and can explain the disparity in the transition region by increasing the reaction selectivity towards direct oxidation.

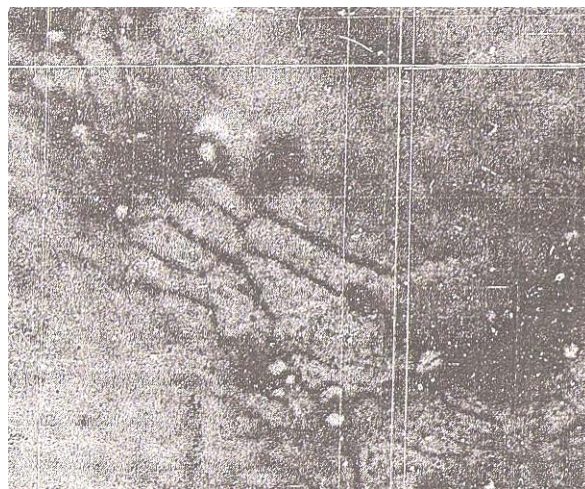


Figure 2.16 UC_x Cracks in UO₂ Layers [Stobbs and Whittle (1966)]

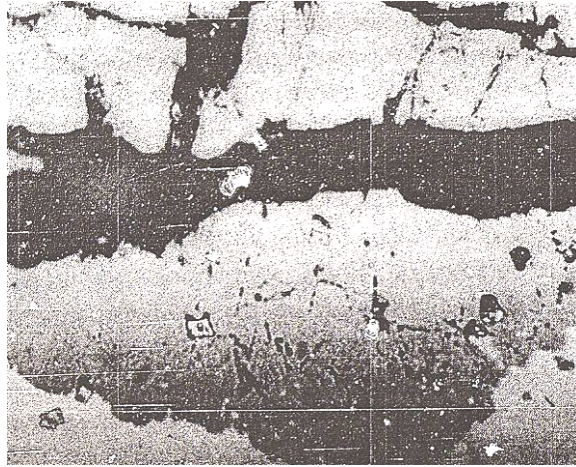


Figure 2.17 UC_x Cracks in U₃O₈ Layers [Stobbs and Whittle (1966)]

Carbide inclusions are common in cast pieces and rolled parts due to the presence of graphite and the translation of carbon into the fluorite lattice [Stobbs and Whittle (1966)]. This can explain why the wires ignited at higher temperatures than the cubes and foils in the Baker et al experiments [Baker et al (1966)]. With respect to Equation 1 this increases the heat generation term and decreases the convective and radiant heat transfer leading to an increase in $\partial T/\partial t$. Due to the difference in the crystal lattice, the concept of carbide nucleation of oxide formation has been discounted [Stobbs and Whittle (1966)]. However, the carbide inclusion as a separator between the oxide layers does serve to increase the division of the oxide particulate and could increase the amount of airborne particulate entrained in the oxide fume. Since uranium carbide will not oxidize, the carbide inclusions separate from the surface once the surrounding material has been oxidized. Subsequently, the uranium carbide forms a solitary particle of diameter equivalent to the size of the initial inclusion. Given the small diffusivity of carbon in uranium and the relative small amount of carbide in uranium forms, this contribution is assumed to be negligible for the airborne particulate fragmentation, but is important in determining ignition characteristics in the transition region.

CHAPTER 3 - Fires Involving Uranium Metal

For materials that will not reach an ignition temperature, the oxidation is dependent on the thermal stress imparted by the environment. The primary mechanism for this is a fire in a facility containing uranium metal. Facility fires introduce new variables including burn durations, combustion products, and temperature fluctuations which impact the total oxidation. Each of these parameters and their potential implications will be generally discussed.

Although chips, fines, and turnings with large specific areas can ignite at lower temperatures (e.g. 250 °C), these fires are unable to sustain oxidation of the larger forms like ingots [Elder and Tinkle (1980)]. Since even small facility fires can easily elevate temperatures past the ignition point for these forms (i.e. chips, turnings, and fines) the subtleties of the durations, combustion products, and temperature fluctuations will not be explored for these materials.

3.1. Combustion Product Interactions with Uranium Oxidation

Taking a simplistic view of combustion, the process of combustion will deplete the oxygen content of the atmosphere to a certain extent. This will generate various amounts of carbon monoxide and carbon dioxide depending on the burn duration. The simplest representation of incomplete combustion is shown as Equation 3. This generates some other combustion products that can influence the oxidation of uranium.

Equation 3 Simplistic Combustion Equation

Combustion yields $C_nH_{2n+2} + \delta O_2 \rightarrow \alpha CO + (n-\alpha) CO_2 + (n+1) H_2O$ where $\delta = \frac{1}{2}(3n - \alpha + 1)$.

There are three products of the combustion reaction that contain oxygen that could potentially be available to oxidize uranium. Some of these compounds will also compete with uranium for available oxygen impacting the reaction progression by decreasing the oxygen concentration, denoted within $\partial w/\partial t$ in Equation 1. Since the quantity of each product cannot be quantified for all conditions, the general properties of each product will be discussed.

3.1.1 Acceleration of Oxidation Reactions in the Presence of Carbon Dioxide

Carbon dioxide is the most complete combustion product, stable at full oxidation. However this molecule has a pair of oxygen atoms that can be disassociated. The disassociation of a single oxygen atom from CO₂ has a lower entropy delta (22.1 J/mol·K @ 500 K) than that of disassociating O₂ (48.5 J/mol·K @ 500 K) [Green (2008)]. Therefore uranium, below the ignition point, more readily oxidizes in an enriched CO₂ atmosphere due to the decrease in the energy required to create free oxygen atoms [Tyzak and Cowan (1976)]. In contrast the H₂O generated from combustion has higher disassociation energies {73.9 J/mol·K @ 500 K [Green (2008)]} and uranium will not compete for the oxygen in H₂O at elevated temperatures {e.g. > 100 °C [Megaw et al (1961)]. This accelerates the oxidation of uranium metal in a CO₂ enriched atmosphere [Elder and Tinkle (1980), Megaw et al (1961), and Schnizlein et al (1959)].

3.1.2 Retardation of Oxidation Reactions in the Presence of Carbon Monoxide

Carbon monoxide is a major competitor with uranium for free oxygen in a system. With competing reactions, the rate kinetics are retarded. From experiment the observation has been made that the oxidation of uranium may be stopped in the presence of carbon monoxide [Wang et al (1996)]. Carbon monoxide has a lower free energy than some uranium oxide states and higher than other oxide states dependent on localized temperatures. Based on available phase diagrams, the free energies equalate whereby CO exists as an intermediate to CO₂, with multiple uranium oxide interactions to be considered [Wang et al (1996)].

Considering all the oxides of uranium singularly simplifies the system into a ternary competition for oxygen. Carbon monoxide competes for oxygen with uranium oxides while the uranium oxides are capable of stripping an oxygen from CO₂ which increases the CO concentration and slowing the ability of uranium to obtain free oxygen. Depending on the oxidation state of uranium, CO may have sufficiently lower entropy to stop the oxidation reaction at certain concentrations and temperatures [Wang et al (1996)]. This technique can be used in the treatment of uranium to help form a solid protective UO coat on the material retarding air oxidation at temperatures up to 600 °C [Watts and Cayless (1961)]. The presence of CO therefore has a direct reduction on the $\partial w/\partial t$ term in Equation 1. Subsequently uranium, both above and below the ignition point, will oxidize more slowly in an enriched CO atmosphere.

3.2. Potential Worst Case Fire Scenarios

For simplification, a large building fire is a combination of multiple localized fires. The localized fire determines the oxidation potential, which determines the characteristics of the oxide fume and aerosol. Fires will be segmented into three types, colocated storage of combustibles, transient fire hazards, and process equipment hazards. Each will be looked at to determine the general temperatures that can be anticipated.

Starting with colocated storage of combustible material, the burning durations and the potential heat release are compared. Using NUREG-1805 Chapter 8 [Iqbal and Salley (2004)] for estimating the burning duration of solid combustibles a stack of wooden pallets 10 high (48-inch square) would burn for 5.24 minutes after ignition. This configuration has a combustible loading of 30 lbs/ft² corresponding to the NFPA severity rating of “Severe”. A stack of Ultra-High-Molecular-Weight (UHMW) polyethylene sheets (0.930-0.935 g/cm³) 2 ft x 2 ft x 1 ft high could burn for 2.6 hours. This configuration has a combustible loading of 58 lbs/ft² which would indicate a complete and total breakdown of combustible material control programs used to demonstrate compliance with NFPA fire code and fire ratings [Steciak et al (1983)].

In addition to solid combustible material, there is potential for liquid fuel pool fires which have larger heat releases. NUREG-1805 Chapter 3 [Iqbal and Salley (2004)] for estimating the burning characteristics of a liquid pool fire indicates that a 55-gallon drum full of diesel fuel that after ignition stays contained by the drum, will burn for a maximum of 4 hours with a maximum flame height of 6.6 feet. Fuel spills have shorter burn durations due to large surface area. For comparison for a 1 ft x 1 ft x 1 ft concrete sump the burn duration could be as high as 1.7 hours. Therefore the worst case heat release rate and duration is diesel fuel at 420.77 kW for 4 hours.

For transient hazards, the most common hazard is a lift truck used to move heavy quantities of material. Many lift trucks have noncombustible construction and fire resistant hydraulic fluids, but older equipment typically does not. Assuming a lift truck with combustible construction and fluids provides a maximum heating value. A review of numerous lift truck fire scenarios calculated using DETACT-QS as published by NIST in FPEtool version 3.2 [NIST (1995)] indicates that the worst case heat release rate is 4,835 kW for 47 minutes [Dungan (2003)].

A process equipment fire is similar to a lift truck fire in complexity, but most machining equipment is essentially steel containing hydraulic fluid, electrical insulation, lubricating oil, and coolant. The combustible hydraulic fluid and lubricating oil are bounded by taking the highest heating value and maximum volume with the surface area of the oil reservoir. NUREG-1805 Chapter 3 for estimating the burning characteristics of a liquid pool fire indicates that 30 gallons of lubricating oil with a surface area of 5 ft², will burn for 1.33 hours with a heat release rate of 346.9 kW. The maximum height of the flame would be 5.4 feet from the surface of the fuel.

The highest heating value is associated with the lift truck fire and the longest duration is associated with the contained liquid pool fire in the storage areas. These heating values and durations will be used to determine the maximum flame temperature and size of that zone as well as the maximum hot gas layer temperature. The worst case potential fire scenario is the lift truck fire due to the heating value dominating oxidation kinetics more than duration.

3.3. Outlining of Zones Corresponding to the Ignition Region

A room segment is necessary to determine hot gas layer temperatures for determining oxidation zones. Since a lift truck should be able to traverse the space, the room segment will need to be large enough for the operation but as small as practical. Standard 2.5-ton lift trucks have mast heights of 17 feet or less, therefore the height of the room will be set to 20 feet to allow for HVAC and lighting spaces above the truck. The length of a 2.5-ton lift truck is between 10 and 15 feet including the tines depending on the model. Including a turn radius of 5 feet plus 5 feet on each side for storage racks gives a nominal width of the space of 30 feet. The length of the space will be set equal to the width.

The space will be insulated with concrete block walls to retain heat for determining hot gas layer temperatures. Only natural ventilation will be assumed. NUREG-1805 Chapter 2.1 for predicting hot gas layer temperature in a room using the aforementioned segment characteristics determines the temperatures shown in Table 3.1. FPEtool is used to determine maximum flame temperature [NIST (1995)]. These calculations assume no fire sprinkler response. From these calculations the lift truck fire is obviously the worst case potential fire scenario.

Table 3.1 Fire Scenario Heat Characteristics (Dungan, 2003)

	Heating Value (kW)	Duration (hr)	Hot Gas Temp (°C)	Max Flame T (°C)
Storage Area	421	4.04	165	778
Transient	4,835	0.78	700	811
Process Area	347	1.33	147	730

The impacts of the fire sprinkler response drop the hot gas layer temperature to under 100 °C and shorten the duration of the fire. Since temperatures under 100 °C are oxygen diffusion controlled reactions with the UO₂ end state, the entire space will be considered a single zone under these scenarios. For the transient fire scenario there will be four zones assumed. The first zone will be the immediate vicinity of the flames where flames may directly impinge uranium. The second zone is the hot gas layer temperature which is at the ceiling of the facility. Immediately beneath the hot gas layer is the smoke layer. Beneath the smoke layer is the floor zone.

The height of each zone and the maximum temperature of the smoke layer and the maximum temperature of the floor zone can be estimated using FPEtool. For the room segment previously defined, the thickness of the hot gas layer is approximately 11 feet. The height of the smoke layer is 7 feet and the height of the floor zone is 2 feet. The flame zone will be assumed to be a 13 ft radius right cylinder originated at the lift truck which can be transient in the room. The maximum temperature of the smoke layer is 500 °C and the floor zone temperature is less than 200 °C.

Looking at reaction selectivity in each zone, the majority of the zones are in the region where the oxidation product is U₃O₈ and the reactions are not diffusion limited. The floor zone is in the upper range where the end state will be a UO₂/U₃O₈ mixture where diffusion kinetics are still present. Uranium with specific areas larger than 1.0 cm²/g will ignite at temperatures over 500 °C, such that chips, turnings, and fines in any zone except the floor zone can ignite and proceed to complete oxidation. The bulk forms of uranium will not ignite in any of these zones. Although bulk uranium will not ignite, the material will oxidize at a given rate, referred to as the burn rate that corresponds to the temperatures in each of the fire zones.

3.4. Burn Rate Relationship to Specific Area

The burn rate is defined as the rate at which the oxidation reaction progresses through a piece of uranium metal, such that the rate can be determined by removal of the oxide layer and comparison to the original dimensions of the piece. This burn rate is dependent on the oxidation rate which is tied to the specific area. The burn rate for uranium with specific areas less than 1 cm²/g can be determined empirically using previous experiments.

The results of the Elder and Tinkle (1980) experiments, which are presented in Tables 3.2, 3.3 and 3.4, allow the development of estimated uranium burn rates. These results indicate a maximum burn rate of 0.152 cm/h from the controlled temperature experiments and a maximum burn rate of 0.235 cm/h from the experiments in which heat was supplied by ten batches of wood and paper packing materials. Fires initially grow to maximum intensity and then diminish in intensity as the fuel is consumed. The maximum uncontrolled temperature burn rate requires an average fuel to uranium ratio of 2.5 to 1, by weight, sustained over the duration of the fire with 2.23 m/s (5 mph) of airflow positioned to maintain the maximum temperature of the fire near the uranium mass [Elder and Tinkle (1980)].

The temperature cycling in the uncontrolled temperature experiments from each of the 10 fuel cycles allowed the β -phase depleted uranium penetrators to routinely slough the oxide layers exposing fresh material to direct oxidation as opposed to diffusion limited oxidation. Since α -phase and γ -phase materials are less brittle and exhibit less expansion/shrinkage due to temperature fluctuations, beta-phase behavior typifies the worst case scenario. These conditions can occur in the hot gas layer, although the temperature fluctuations in the gas layer are not as extreme as those recorded in the Elder and Tinkle burn test # 4 with $\Delta T \approx 500$ °C. The ~ 500 °C temperature fluctuations sustained over minutes lead to the slough of oxide layers and not the creation of airborne particulate. Therefore the burn rate of 0.235 cm/h is not applicable for oxidation generating airborne particulate. The burn rate of 0.152 cm/h derives from air flow and ambient temperature control which exceed the conditions anticipated to be present during a worst case facility fire due to the relatively high gas face velocity, the presence of smaller nominal specific areas, and metallurgical phase changes (e.g. alpha to beta) which increases the potential for generation of airborne particulate.

The aluminum containers used for the DU penetrators were omitted from the Elder and Tinkle experiments since the melting point of aluminum (650°C) was below the experimental temperatures, however the 304 stainless steel containers typically used for modern storage have a melting point higher than uranium (1400-1425 °C). The majority of uranium during any large fire scenario will be containerized to some extent limiting the surface area for oxidation. Containerization is employed both for contamination control, personnel handling considerations, and quality of the material. Noncombustible racks and other storage methods also function to reduce the total airflow, in proximity to uranium, to levels anticipated to be significantly less than the experimental conditions.

The third factor is the duration of the large fire. Using data from Table 3.5, fires involving bulk material need durations in excess of 8 hours to oxidize 0.5 inches of material which are beyond the durations of any fire scenario as shown in Table 3.1. Given the plausible fire scenarios, the results presented in Table 3.2 are judged to be the best available information applicable to facility fires and sufficiently conservative to provide a significant margin of safety when applied to fires involving uranium with specific areas less than 1 cm²/g. The data in Table 3.3 are useful in oxygen limited fires; however the maximum burn rate from Table 3.2 is the limiting case.

Based upon the results of the Elder and Tinkle experiments, a maximum burn rate of 0.152 cm/h is used [Elder and Tinkle (1980)]. The burn rate can also be expressed as a burn rate in g/h-cm² by multiplying the 0.152 cm/h burn rate by the uranium alloy density of approximately 18.9 g/cm³. Therefore, the burn rate of 0.152 cm/h is equivalent to a burn rate of 0.152 cm/h × 18.9 g/cm³ or 2.87 g/cm²-h. Given a burn duration of 2 hours, only uranium with a specific area greater than 1.4 cm²/g could completely oxidize without ignition. Given the previously defined fire zones, these forms would ignite and completely oxidize regardless of fire duration. For bulk uranium forms, the maximum oxidation can therefore be determined by the smallest characteristic dimension of the piece. Table 3.5 provides example burn durations for characteristic lengths of ¼ to 4 in. based on a 0.152 cm/h burn rate. These burn rates can be applied to any geometry through the use of the characteristic dimension given a specific area less than 1.0 cm²/g.

Table 3.2 Controlled Temperature, in Air, Results From Elder and Tinkle (1980)

Burn Temperature (°C)	Atmosphere	Burn Time (h)	% Oxidized	% Aerosol	% Respirable	ARF ^a	RF ^a	ARF _x RF	Burn Rate ^b (cm/h)
500	Air	2	6.80	2.2E-04	1.0E-05	3.2E-05	0.04545	1.5E-06	0.045
600	Air	2	6.20	1.6E-04	1.7E-05	2.6E-05	0.10625	2.7E-06	0.041
700	Air	2	22.10	1.9E-03	5.7E-05	8.6E-05	0.03000	2.6E-06	0.152
800	Air	2	17.60	9.0E-04	3.7E-05	5.1E-05	0.04111	2.1E-06	0.119
900	Air	2	15.70	3.3E-03	3.8E-04	2.1E-04	0.11515	2.4E-05	0.106
Arithmetic Means						8.1E-05	0.06759	6.6E-06	0.093
Geometric Means						6.0E-05	0.05851	3.5E-06	0.081
Maximum Values						2.1E-04	0.11515	2.4E-05	0.152

Table 3.3 Controlled Temperature, with CO₂, Results From Elder and Tinkle (1980)

Burn Temperature (°C)	Atmosphere	Burn Time (h)	% Oxidized	% Aerosol	% Respirable	ARF ^a	RF ^a	ARF _x RF	Burn Rate ^b (cm/h)
500	50%air 50%CO	2	6.00	2.5E-04		4.2E-05			0.039
600	50%air 50%CO	2	6.30	4.5E-04	2.5E-05	7.1E-05	0.05556	4.0E-06	0.041
700	50%air 50%CO	4	21.30	5.8E-03	8.5E-04	2.7E-04	0.14655	4.0E-05	0.073
800	50%air 50%CO	4	30.10	1.5E-03	2.3E-05	5.0E-05	0.01533	7.6E-07	0.106
900	50%air 50%CO	4	24.90	7.5E-04		3.0E-05			0.086
1000	50%air 50%CO	4	23.60	1.1E-02	7.9E-04	4.7E-04	0.07182	3.3E-05	0.082
Arithmetic Means						1.8E-04	0.07231	2.0E-05	0.078
Geometric Means						1.1E-04	0.05472	8.0E-06	0.074
Maximum Values						4.7E-04	0.14655	4.0E-05	0.106

^a ARF = (% Aerosol) divided by (% Oxidized) and RF = (% Respirable) divided by (% Aerosol).

^b The Burn Rate is calculated by using an initial diameter equal to 2.59 cm and assuming that the length is approximately constant. (Final Mass) / (Initial Mass) = (Final Area) / (Initial Area) = [(Final diameter) /

$$(\text{Initial Diameter})]^2 \text{ and } \frac{d(\text{diameter})}{d(\text{time})} = \frac{(\text{Initial Diameter})}{(\text{Burn Time})} \left(1 - \sqrt{1 - \frac{\% \text{Oxidized}}{100}} \right).$$

Table 3.4 Uncontrolled Temperature Results From Elder and Tinkle Experiments (1980)

Burn Temperature (°C)	Atmosphere	Burn Time (h)	% Oxidized	Burn Rate ^b (cm/h)
700 to 900 ^(a) (10 batches of fuel)	Air	3	44	0.217
			47	0.235
			42	0.206
Arithmetic Mean				0.219
Geometric Mean				0.219
Maximum Value				0.235

^aThe average bulk temperature range during the experiment was 700 to 900°C while 10 batches of fuel was added to the fire with local temperatures intermittently exceeding 1400°C. Information is not available to calculate the ARF, instead a bounding ARF was calculated using a single filter stage and extrapolating that to get a bounding ARF = 7.8E-4 / RF = 0.62. The high respirable fraction is believed to have resulted from the thermal cycling while fuel was consumed and then added which allowed the protective oxide layer to break away exposing fresh metal.

^bThe Burn Rate is calculated by using an initial diameter equal to 2.59 cm and assuming that the length is approximately constant. (Final Mass) / (Initial Mass) = (Final Area) / (Initial Area) = [(Final diameter) /

$$(Initial\ Diameter)]^2 \text{ and } \frac{d(diameter)}{d(time)} = \frac{(Initial\ Diameter)}{(Burn\ Time)} \left(1 - \sqrt{1 - \frac{\% \text{ Oxidized}}{100}} \right).$$

Table 3.5 Example Burn Durations for a Burn Rate of 0.152 cm/h (DOE 1994).

Thickness (in)	Thickness (cm)	Burn Duration (hr)
0.125	0.32	2.1
0.25	0.64	4.2
0.5	1.27	8.4
1	2.54	16.7
2	5.08	33.4
4	10.16	66.8

3.5. Maximum Oxidation of Uranium Forms.

Using the duration of the bounding fire scenario and the maximum burn rate allows for the determination of how the oxidation may progress into the uranium form. A characteristic dimension of 0.12 cm (3/64th inch) applies to the oxidation of uranium forms under the postulated fire scenario that includes decay of the fire to extinction. This burn rate is used to determine the maximum oxidations shown below in Table 3.6. As shown for facility fires, typically less than 10% of the inventory could oxidize via these burn rates.

Table 3.6 Maximum Oxidation of Uranium Forms

Designator	Initial Mass (g)	Final Mass (g)	Percent Oxidation
M829A1	7,343	6,691	8.88%
PGU-14/B	300	249	17.13%
XM774	3,355	3,041	9.37%
XM900E1	4,552	4,023	11.61%
1 x 2 x 2 block	1,239	1,125	9.17 %
1 x 2 x 3 block	1,000,000	989,385	1.06 %
1 x 3 x 5 block	4,646	4,315	7.11 %
1 x 5 x 7 block	10,840	10,161	6.26 %
2 x 3 x 4 block	7,433	7,059	5.03 %
Geometric Average			6.91%

NOTE: Designators are from Table 2.1 and Table 2.2

* Data from Chambers et al (1982), Elder and Tinkle (1980), Glissmeyer and Mishima (1979), Hanson et al (1974), Jette et al (1989), and Mishima et al (1985)

Uranium metal has no release fractions since only the oxide forms develop airborne particulate. The oxide fume will focus on the portion of the oxide that separates from the surface of the material and will apply to material that sustains oxidation upon ignition. Therefore the aforementioned 10% maximum oxidation is an intrinsic damage ratio that can be applied to bulk metal storage forms separate from the release fractions that will be discussed based on the characteristics of the oxide fume and aerosol dispersal. The qualitative impact is that non-ignitable uranium forms, e.g. those with specific areas less than 1.0 cm²/g should have total release fractions at least one order of magnitude smaller than ignitable forms. The information presented thus far demonstrates that the release from bulk uranium forms is an order of magnitude less than that from the chips, fines, and turnings.

CHAPTER 4 - The Oxide Fume

The oxide fume is the portion of the oxide particulate that separates from the surface of the uranium metal and can be suspended in the surrounding gas. The oxide fume is inclusive of the stable aerosol and unstable entrained particulate. Small particulate can be entrained based on the velocity of the gas at the surface. The term aerosol is used to define the system consisting of fine particles in gaseous suspension [DOE (1976)]. Here the aerosol is the system containing oxide particulate with aerodynamic equivalent diameters (D_{AE}) less than 10 micrometers (μm).

The oxide fume contains particulate that may exceed 100 μm D_{AE} which is at the lower end of the visible range [DOE (1976)]. The oxide particulate of a size greater than 30 μm D_{AE} does not stabilize in gaseous suspension. The primary difference between the oxide fume and aerosol is that the aerosol is a stable system. The oxide fume as an entity generally tries to fall out of gaseous suspension as the thermal buoyancy of the fume changes.

4.1. The Creation of Oxide Particulate

Oxide particulate is a consequence of the oxidation reaction. The particulate is generated via two principal mechanisms, either mechanical stress/strain or direct chemical oxidation. The progression of oxidation through the metal determines which of these mechanisms generates the particulate [Connors and O'Neil (1954)]. The mechanism of generation has considerable impact on the final dimensions of the particulate [Iwasaki et al (1969)]. These mechanisms are dependent on the specific area for selectivity which is observable by pyrophoric properties. Direct chemical oxidation is typically indicated by pyrophoric sparking.

Mechanical stress/strain under diffusion limited reactions is dependent on the density changes of the oxide layers and the crystalline structure transformation in the material. The progression of reactions under pyrophoric conditions or above the ignition temperature shifts the dominating forces of the oxidation and generates particulate that can more readily aerosolize [Coleman and Schwendiman (1962)]. These factors determine how the aerosol will be generated which has significant impact on the subsequent equilibrium and dispersion characteristics.

4.1.1 The Progression of Oxidation Through Uranium Metal

The rate of the oxidation influences the stress impacted on the uranium metal. Above the ignition temperature where direct oxidation of material proceeds rapidly, oxide is produced in non-adherent states that create particulate [Coleman and Schwendiman (1962)]. Specifically the lack of significant adherent states like $\text{UO}_{1,X}$ and $\text{UO}_{2,X}$ results in the disassociation of UO_2 and U_3O_8 from the UO layer which accelerates oxidation of the UO layer [Colmenares et al (1981)]. Depending on the local temperature UO_2 may or may not convert to U_3O_8 , but the crystal structure change associated with that conversion can divide the UO_2 into finer U_3O_8 particulate then the separation of U_3O_8 as a single oxide layer [Iwasaki et al (1969) and Iwasaki and Nishikawa (1970)]. At ignition temperatures, or the maximum temperature of the hot gas layer, the final oxide particulate is almost exclusively U_3O_8 . This is observed as the particle size of U_3O_8 tends to decrease as temperature increases [Chambers et al (1982), Coleman and Schwendiman (1962), Glassner (1957), Hilliard (1958), and Isaacs and Wanklyn (1960)]. Particulate separating as a uniform lattice is larger than a lattice undergoing transformation which separates under vigorous reaction [DOE (1976)].

Comparatively, at temperatures below ignition, diffusion dominated oxidation produces the adherent oxide states like $\text{UO}_{1,X}$ and $\text{UO}_{2,X}$. These states require mechanical stress/strain to generate particulate. The primary source of stress is the volumetric expansion and contraction of the oxide density which reduces the cohesion between oxide layers. The speed of the reaction on a micro-scale must be taken into consideration whereby the gradients of the change, especially temperature fluctuations that change reaction selectivity, must be taken into account. Each of these mechanical stress initiators will be handled separately on a level equally as important as the progression of the oxidation reaction.

4.1.2 The Impacts of Density Changes Associated With the Oxidation of Metal

The volumetric expansion and contraction of the oxide layers introduces various stresses in uranium. The existence of the intermediate oxides $\text{UO}_{1,X}$ and $\text{UO}_{2,X}$ are unique in that these states are denser than the higher and lower oxidation states. The expanding lower-layer stretches the lattice of the intermediate oxide layer until the surface fractures relieving the strain. This increases the surface roughness of the intermediate layer.

The upper-layer expands faster than both the sub-layer and the intermediate layer such that upper and lower layers with oxide states having different crystalline structures can interact. When the expanding upper-layer covers the surface roughness gaps in the intermediate layer, oxygen or other gases are trapped in the crevice. The competition for oxygen molecules between the oxides typically results in the lower oxidation state oxidizing and releasing heat [Cubicciotti (1952)]. This expands the gases in the crevice which introduces strain underneath the upper oxide layer. When coupled with the volumetric expansion of this layer, pieces of the upper oxide layer over the crevice can easily be displaced generating oxide particulate [Isaacs and Wanklyn (1960)].

Complicating matters is the fact that local temperature is a function of the heat release from the exothermic oxidation reactions, which is different from the bulk modulus temperature of the gas layer as indicated in Figure 4.1. The change in density of the lower-layer causes the deformations in the intermediate oxide layer to contract which can introduce shrinking stress resulting in the displacement of oxide particulate. Notably the shrinking causes displacement of larger particulate than the expansion of gases during the expansion process.

The change in the density of the oxide layer is the principal factor in determining generation of oxide particulate from mechanical stress. The incremental differences between the nominal densities of each oxide state increase as temperature increases such that the density delta is higher at higher temperatures [Isaacs and Wanklyn (1960)]. Subsequently the impacts of the density changes increase proportionally to the delta in the temperature fluctuations. As shown in Figure 4.1, temperature fluctuations in excess of 50 °C occur on non-ignitable forms. This is in comparison to temperature fluctuations in excess of 200 °C occurring after ignition as shown in Figure 2.13. Large temperature deltas (i.e., > 50 °C) are observed with the sloughing of large oxide pieces (e.g., millimeter to centimeter diameters). This exposes large amounts of lower oxidation state material to oxygen. Large amounts of energy are subsequently released as the oxidation state increases exothermically. This leads to a temperature spike which can be observed in both air and inert atmospheres [Elder and Tinkle (1980)].

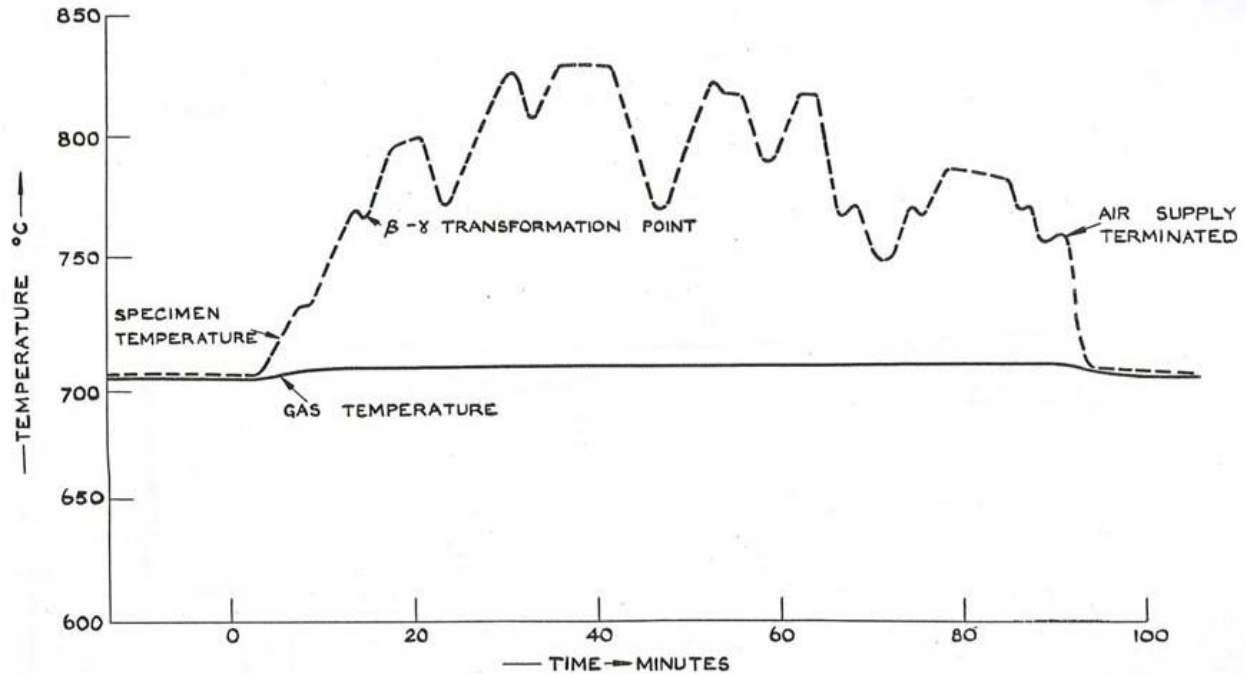


Figure 4.1 Uranium Oxidation Profile at Constant Gas Temp. [Isaacs and Wanklyn (1960)]

4.1.3 Crystalline Structure Impacts on the Oxidized Metal

Crystalline structure changes in the material are the cause of the density shifts due to the contraction of the cubic lattice in the intermediate oxide states before shifting to orthorhombic in the higher oxidation states. The $UO_{2,x}$ intermediates are extremely important existing in two phases that each communicates with the different lattices. During slow oxidation, these intermediates have time to form, introducing a cohesive bond between the layers generating less oxide particulate separation. Faster reactions eliminate some of the intermediates and at higher temperatures the primary interface between UO_2 and U_3O_8 is U_2O_5 , which is significantly less stable than the other intermediate oxidation states.

At higher temperatures the rapid progression of the oxidation allows UO_2 and U_3O_8 to separate from the uranium metal. Since U_3O_8 is the end state at most temperatures and the U_3O_8 to UO_3 progression is slow and reversed at very high temperatures; the U_3O_8 particulate is very stable and the crystalline structure fluctuations of minor impact. However, as UO_2 is exposed to oxygen as a separate particulate, the transition to U_3O_8 requires a structure transformation. Since this reaction does not progress at temperatures less than 190 °C, and is almost instantaneous at

temperatures in excess of 250 °C for particulate, the window where intermediate oxides form is relatively small. Where $\text{UO}_2 \cdot \text{U}_3\text{O}_8$ mixture particulate is formed, the observations have been that the mixture is extremely adherent with larger particulate (e.g. $> 10 \mu\text{m } D_{\text{AE}}$). These observations are the basis for determining the existence of U_2O_5 in measurable quantities once the mixture is cooled and subjected to x-ray analysis.

At local temperatures exceeding 250 °C, UO_2 undergoes a rapid structure change to U_3O_8 . Observation of this transformation indicates that the lattice structure loses cohesion dividing the UO_2 particulate into smaller U_3O_8 particulate [Aronson et al (1957)]. The structure changes causing the separation have not been directly observed since the reaction progresses more rapidly than the x-ray analysis techniques can determine the structures. This temperature plateau also indicates that upon ignition the UO_2 layer is separating from the uranium metal [Isaacs and Wanklyn (1960)]. After the ignition temperature has been reached, for those forms with ignition temperatures, the reaction progresses rapidly forming finely divided U_3O_8 particulate (e.g. $< 10 \mu\text{m } D_{\text{AE}}$). This particulate can be subsequently entrained as an aerosol. Therefore the change in the crystal lattice structure is a key mechanism in the generation of aerosol.

4.1.4 The Relationship Between Pyrophoricity and Aerosol Generation

Pyrophoricity is defined as the point where the material emits sparks or ignites spontaneously. When used in reference to uranium oxidation, pyrophoricity is the point where sparks can be observed. This is often considered as localized ignition of the uranium particulate although typically observed only on materials with specific areas greater than $1 \text{ cm}^2/\text{g}$. These shapes have large surface areas to allow for diffusion of oxygen and small uranium mass to absorb the thermal stress of the exothermic oxidation [Gittus (1963)]. The oxidation reactions can therefore progress rapidly at room temperature resulting in shedding of the UO_2 oxide layer.

The shedding of this layer is stable if the local temperature is less than 190 °C, but the excess energy of oxidation can easily raise local temperatures much higher, following the trends shown in Figure 2.13 and Figure 4.1 with local temperatures more than 100 °C higher than ambient conditions. This allows the oxidation of the particulate to proceed from UO_2 to U_3O_8 releasing more heat and has a tendency to generate smaller particulate. This heat also increases the rate of

oxidation on the colocated piece that generated the original particulate unless there is an alternative material to absorb the heat. The extent of the oxidation can either accelerate or retard the reaction since uranium oxide acting as a heat sink often quenches further reaction. This is noticeable with masses where large amounts of oxide are generated and extinguishing reactions. Nonetheless materials that are pyrophoric will generate aerosol and the incremental release of energy can transition the entire uranium piece past the ignition point for that shape.

4.2. Equilibrium of the Aerosol

The aerosol is the stable or quasi-stable suspension of oxide particulate in the gaseous phase. The gaseous phase of concern is typically air and the quasi-stability of the aerosol is dependent on both temperature and relative velocity. The lower stability of the aerosol is the point where the suspension of material can be maintained at ambient conditions [DOE (1976)]. For aerosol in the uranium oxide fume, there are essentially three materials of concern, UO_2 , U_3O_8 , and $\text{UO}_2 \cdot \text{UO}_{2,x} \cdot \text{U}_3\text{O}_8$. The size and quantity of these species is dependent on the temperature of the oxidation reaction. For the condition where the intermediate oxide states are present, there is an equilibrium phase shift that can occur. Additionally there is an affinity for the formation of hydrates and other compounds that drop out of suspension as the temperature decreases in the oxide fume. Each of these three traits will be briefly discussed in additional detail.

4.2.1 The Relationship Between Structure and Temperature of Oxidation

The localized temperature of the oxidation has the greatest impact on the aerosol formation. Low temperature oxidation results in UO_2 and a primarily UO_2 aerosol while high temperature oxidation results in U_3O_8 and a U_3O_8 aerosol. The intermediate range where the oxide is a mixture with a particulate generation that is a mixture of UO_2 , $\text{UO}_{2,x}$, and U_3O_8 compounds has a general trend that shifts to the respective end state of the principal oxide at that temperature.

During the chemical recovery of the oxide the UO_2 and intermediate mixture have been dubbed “low temperature oxides”. The chemical recovery involves the dissolution of oxide particulate in acid, typically nitric acid. The face-centered cubic and transitional lattice interacts with the acid, easily dissolving the oxide. The “high temperature oxides” are primarily U_3O_8 in the tight packed orthorhombic state which are much more difficult to dissolve in acid. This characteristic of the various oxides’ ability to interact with other ions determines whether or not the particulate

will form an intermediate and fall out of solution. The general trend is that the higher the temperature, the higher the oxidation state, and the lower the probability of the change in particulate size once the aerosol is formed. The complications arise from the size of the particulate generated at these temperatures since larger particulate is more likely to gravimetrically settle out of solution.

4.2.2 The Associations Between D_{AE} and Oxidation State.

The aerodynamic equivalent diameter (D_{AE}) of the particulate generated is tied to oxidation state through the mechanisms used to generate that particulate. Higher oxidation states are the product of higher temperatures, but intermediate temperatures (190 °C to 225 °C) produce oxide mixtures which can phase shift between the oxidation states and are more prone to disassociation of the particulate [Coleman and Schwendiman (1962)]. Low temperature oxidation (< 190 °C) has not been observed to generate aerosol unless the material is pyrophoric, whereby the aerosol is generated at undetermined local temperatures that most likely exceed 190 °C. The smallest D_{AE} particulate is generated either through the pyrophoric reaction or from the disassociation of particulate in the intermediate temperature range. These particles have been observed through microscopy on filter media in the range of 0.3 μm to 10 μm D_{AE} where the filter media was collected using a cascade impactor [Mishima et al (1985)].

High temperature oxidation (> 225 °C) has a tendency to generate a large distribution of particulate in the 10 μm to 100 μm D_{AE} range with the average size near 30 μm D_{AE} as determined by sieve analysis and precutter masses on cascade impact filters [Mishima et al (1985)]. Significant data are available on high temperature oxide formation and this product is the anticipated result of a facility fire during the incipient stages. The determining factor on the particulate size is the speed of the oxidation. Faster oxidation has been observed to generate smaller particulate as evident by the same analysis while slower oxidation has been shown to clog many of the precutter and sieve filters through a predominance of the larger particulate size [Mishima et al (1985)]. Subsequently there is no direct correlation between the oxidation state and D_{AE} and currently no models have been able to correlate or predict the responses observed in the experiments that measured the D_{AE} distribution of the aerosol.

4.2.3 The Reactions of the Oxide Fume as Temperature Decreases

The conversion of UO_2 to U_3O_8 is irreversible at temperatures less than $1250\text{ }^\circ\text{C}$, with no equilibrium phase shift except in the intermediate temperature range ($190\text{ }^\circ\text{C}$ to $225\text{ }^\circ\text{C}$). The loss of external thermal energy slows the oxidation resulting in a disassociation of the particulate at the interface of the crystalline structure transformation. As temperature decreases there are essentially UO_2 and U_3O_8 particulate in equilibrium with air [Coleman and Schwendiman (1962)]. The ratios of these two oxides are neither constant nor linear with temperature due to the decomposition of U_3O_8 at temperatures over $1250\text{ }^\circ\text{C}$. Correlating the chemical oxidation state of the particulate and the ignition characteristics is difficult due to the large temperature fluctuations. However the correlation between ignition and particulate size is that ignited forms produce finer particulate which measures primarily as U_3O_8 .

Each of the oxides has a substantial positive charge that allows for ionic interactions with other compounds in the gaseous phase. There is the potential for ionic bonds to form if oxides are in sufficient proximity, but the mean free path and relative concentration of uranium oxides in the aerosol are not conducive to this interaction. However the combustion products mentioned in section 3.1 are present in the oxide fume as the temperature decreases. There are no known oxy-carbon states of uranium, only oxides and carbides indicating there is no reaction between CO and CO_2 with the oxide particulate. Uranium oxide hydrates are known compounds that are stable in solid form at temperatures less than $100\text{ }^\circ\text{C}$ indicating that there may be potential interaction with the H_2O combustion product.

Within the oxide fume there are significant temperature fluctuations that can facilitate the formation and disassociation of hydrates. Hydrates of uranium oxide are not considered to be stable in the aerosol and typically settle gravimetrically out of the oxide fume. The higher positive charge on UO_2 increases the affinity for this oxide to preferentially select to hydrate in large quantities, but the mean free path of the oxide particulate and the concentration gradients most likely negate this preference within the oxide fume for particulate $< 30\text{ }\mu\text{m } D_{\text{AE}}$. This bonding affinity can explain why particulate $> 30\text{ }\mu\text{m } D_{\text{AE}}$ settles out of gaseous suspension within the first few seconds of generation. Therefore the hydration of oxide fume is assumed to be more of a function of particulate size than oxidation state.

4.2.4 Characteristics of the Aerosol at Equilibrium

The critical point of interest regarding the oxide fume is the point where the aerosol is stabilized in the temperature range that can be inhaled by living organisms without the temperature effects of the inhaled particulate causing infinitely more damage than the toxicological and radiological effects of the material. There is disagreement on the temperature at which this occurs, but for general purposes 100 °C gas is assumed to be a reasonable reference point.

The upper range of the quasi-stability of the uranium aerosol is 30 μm D_{AE} which requires a gas velocity in excess of 223 cm/s (5 mph) [Carter and Stewart (1970), Coleman and Schwendiman (1962), and Elder and Tinkle (1980)]. Stability of the aerosol under calm conditions is 10 μm D_{AE} taking into account the nominal turbulence effects of micro-currents and eddies. The difference in the aerosol concentrations under both conditions has been observed such that the stable aerosol may be less than 10% of the quasi-stable aerosol irrespective of dispersion. These characteristics are near the human respirable range where 10 μm D_{AE} is the upper limit for human inhalation as depicted in Figure 4.2. Size distribution is measured by stages on a cascade impactor [Tisch (2006)] to replicate distribution of the aerosol in the human respiratory system.

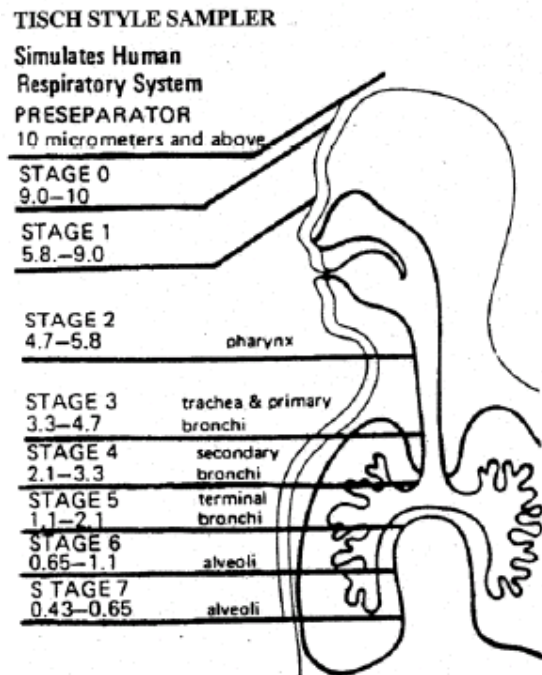


Figure 4.2 Particulate Size Distribution in Human Lungs [Tisch (2006)]

This page intentionally left blank.

CHAPTER 5 - Initial Dispersion of the Oxide Fume

Dispersion is a complex subject that has numerous environmental variables that impact the changes in the oxide fume. This discussion will be limited to the separation of the aerosol from the oxide fume as the fume disperses through thermal buoyancy, diffusion, and settling. The larger particulate in the fume that is not stable in the aerosol will settle out at distances less than 100 meters during which time the oxide fume is subject to Gaussian dispersion. Gaussian dispersion will be handled separately since the aerosol also disperses, albeit the principles of Gaussian dispersion principally apply to solely the aerosol. A look at the temperature gradient anticipated over this distance will be used to correlate to the temperature response of the aerosol and reactions as previously discussed. The differences in the oxide fume and the aerosol as the temperature decreases below 100 °C are also discussed.

5.1. Gaussian Dispersion at Distances Less Than 100 Meters from the Origin

The atmospheric transport of the oxide fume results in a concentration gradient with respect to distance from the release point. A reference distance of 100 meters is chosen as the nominal minimum distance from a point source release to the edge of an emergency response boundary for DOE and NRC facilities [ANSI (1998), DOE (1994), SAIC (1998)]. The mathematical model most commonly used for calculating transport is the Gaussian model. This model is based on the assumption that at any distance downwind of the release point, the material concentration in the plume is normally distributed in the horizontal and vertical directions perpendicular to the wind direction with a maximum value at the plume centerline. This model, as shown in Figure 5.1, has been employed to model plume behavior since 1932 [Hanna et al (1982)].

Key to the Gaussian model is the normal distribution of the plume which is why primary concern is with the aerosol portion of the oxide fume. Larger particulate in the oxide fume do not have normal distributions due to the predominance of gravimetric settling as discussed in Section 5.2. The input source concentration for a Gaussian model needs to be determined from the release fraction generating the aerosol in order to determine the dispersion at any given distance. The basic equation using the Gaussian model for calculating the relative air concentration due to a continuous plume release at a point off the plume centerline is shown in Equation 4.

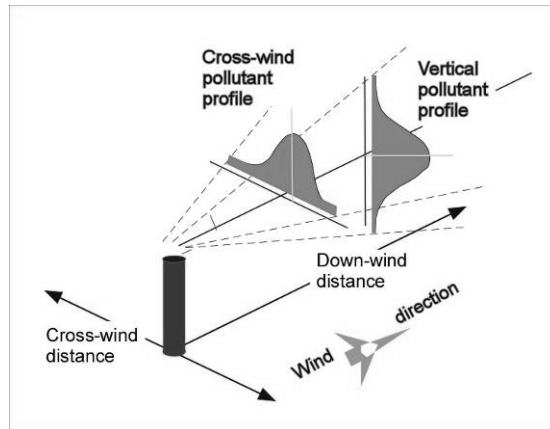


Figure 5.1 Gaussian Dispersion Model (Hanna et al, 1982)

Equation 4 Gaussian Dispersion Equation

$$\frac{\chi}{Q} = \frac{1}{2\pi\sigma_y\sigma_z u} \exp\left\{\frac{-y^2}{2\sigma_y^2} \left[\exp\left(\frac{-(z-h)^2}{2\sigma_z^2}\right) + \exp\left(\frac{-(z+h)^2}{2\sigma_z^2}\right) \right]\right\}$$

- Where: χ/Q = dispersion factor for determining relative air concentration
- σ_y = horizontal crosswind standard deviation of concentrations
- σ_z = vertical standard deviation of concentrations
- u = average wind speed
- y = crosswind distance from the plume centerline
- z = elevation of the dose point
- h = effective release height

Equation 4 can be simplified considerably if the elevation of the receptor is set equal to the release height which maximizes the concentration at the point of exposure. The standard deviations of wind speed have been categorized by the U.S. Environmental Protection Agency into stability classes A-F, with corresponding average wind speeds [Hanna et al (1982)]. General application is that at distances ≤ 100 meters the majority of locations will be F-stability with 1 m/sec wind speeds. This behavior has been confirmed numerous times using cumulative probability distributions of actual meteorology data. Using NUREG-1140 the average resultant behavior is that over the first 100 meters, the value of the χ/Q is approximately $3.5E-3 \text{ s/m}^3$ indicating that the oxide plume concentration will decrease significantly solely by diffusion before other characteristics of the oxide fume are considered [McGuire (1988) and SAIC(1998)].

The most important factor is the qualitative impact of the order of magnitude of the Gaussian dispersion. The χ/Q is multiplied by the source term which is determined by the release fractions that generate the oxide fume. This multiplicative relationship has a collateral socio-political impact that has strongly influenced acceptable parameters for the release fractions. For metals, the default value for the airborne release of material has been set at 1E-3, not based on aerosol data, but indicative of the general reduction threshold of 1E-6 for the cumulative effect once dispersion has been taken into account. The general pretext for selection of this value is that given the complexity of the oxide fume and especially the aerosol as discussed in Chapter 4 of this work, the quantity of experiments did not contain sufficient breadth to support smaller values. Nonetheless, Gaussian dispersion is diffusion of the aerosol and does not account for the separation of the aerosol from the oxide fume as larger particulate is no longer suspended.

5.2. Gravimetric Settling / Dry Deposition of the Particulate

The dry deposition of particulate applies to all airborne matter and accounts for the effects of gravity on the mixture. Wet deposition is the effect of water scrubbing out particulate and is generally not accounted for in fumes with temperatures in excess of 100 °C. Dry deposition is typically taken into account as a fixed rate, applying to both the oxide fume and aerosol. The dry deposition rate typically used is 1 cm/s which accounts for the overcoming of Brownian motion and general atmospheric turbulence associated with insoluble particulate less than 30 $\mu\text{m } D_{\text{AE}}$.

The deposition of particulate in the greater than 30 $\mu\text{m } D_{\text{AE}}$ range typically occurs at a much faster rate and is tied to the terminal velocity of the particulate depending on D_{AE} . The distance the particulate must travel to settle is dependent on initial plume buoyancy, effective release height, wind speed, and turbulence. These distributions have been determined by particulate analysis of the ash left from the energetic oxidation of uranium. The largest distances observed for particulate over 30 $\mu\text{m } D_{\text{AE}}$ were seen during the cooking-off of depleted uranium rounds. The debris field was marked off and analyzed by sieve analysis to determine particulate sizes at various distances from the source. No particulate over 20 $\mu\text{m } D_{\text{AE}}$ was observed near the periphery of the field which was 15 ft from the origin [Mishima et al (1985)].

This indicates that for the determination of the source term in Gaussian dispersion, the release fraction needs to be based solely on the aerosol components since larger particulate in the oxide fume is not a significant constituent. Therefore the standard dry deposition of 1 cm/s is appropriate for accounting for gravimetric settling of particulate from the aerosol. However, given a nominal release height in meters, the deposition times can be measured in minutes and hours at which point the aerosol has been transported significant distance from the source given a median nominal velocity of 1 m/s. This time delay also introduces impacts from the cooling of the oxide fume during the dispersion.

5.3. Cooling of the Oxide Fume at Distances Less Than 100 meters.

The maximum hot gas layer temperature from a postulated transient fire from Chapter 2 was approximately 800 °C. The temperature delta between this plume and ambient conditions indicates that the primary heat transfer mechanisms are natural convection and mixing of the gas. This heat transfer mechanism supports the Gaussian dispersion of the plume with the primary mixing layer at the periphery of the fume. At the periphery of the fume the temperature will decrease below 100 °C where additional compounds can form and material supported wholly by thermal buoyancy will settle out of gaseous suspension. Depending on the wind stability and other factors that impacted the Gaussian dispersion, the plume may not experience significant internal mixing allowing the fume to maintain heat for a longer duration.

The periphery of the oxide fume plume is visible due to the formation of water vapor from the combustion compounds in the gas as temperature decreases and from the suspended particulate. As previously discussed, the nominal D_{AE} of particulate in the uranium oxide aerosol is $< 30 \mu\text{m}$ which is significantly less than the smallest visible particulate $\sim 100 \mu\text{m}$. Therefore the uranium aerosol in the oxide fume will not be visible although the water vapor cloud at the periphery may be visible depending on factors like relative humidity and ambient conditions. The principal factor of the cooling of the oxide fume at distances less than 100 meters is the formation of water vapor at the periphery of the plume which can impact the chemical form of the oxides. The cooling of the oxide fume is the basis for the chemical changes of the oxide fume that impact the stability of the aerosol. The cooling of the oxide fume does not significantly impact the Gaussian dispersion of the oxide fume.

5.4. Changes in the Oxide Fume as Temperature Drops Below 100 °C.

Generally the oxide fume reaches equilibrium with the aerosol before 100 meters, thus the changes in the oxide fume as temperature decreases are simply changes in aerosol stability. Significant changes occur in the aerosol as soon as the local temperature drops below 100 °C and water droplets form. The introduction of water vapor significantly increases the localized drag, reducing the local velocity [Jackson et al (1977)]. Local velocities of 223 cm/s are required to entrain uranium particulate up to 30 μm D_{AE} and velocities in excess of 100 cm/s are required to entrain uranium particulate up to 20 μm D_{AE} [Carter and Stewart (1970)]. The formation of water droplets reduces the local velocity to the point where the majority of particulate $> 10 \mu\text{m}$ D_{AE} falls out of suspension from the aerosol. As the uranium aerosol cools below 100 °C, the quasi-stability of up to 30 μm D_{AE} decreases to the stable 10 μm D_{AE} gaseous suspension.

A less quantifiable impact is the scrubbing effects of water droplets as airborne particulate collide with the droplet falling out of suspension and the formation of uranium-oxy-hydrates. The formation of hydrates is a mechanism that relies upon the positive charge of the uranium oxide state and the dipole moment of the water droplet. Both of these molecular interactions are dependent on the intermolecular spacing and the mean free path. Since the concentration gradient of the water droplets is highly dependent on ambient conditions, especially temperature and humidity, this effect is highly variable. This effect has no impact on the formation of the aerosol at the source and is therefore only a modifier to the Gaussian dispersion.

The interactions between the uranium oxide fume and water vapor shift the equilibrium of the final oxidation state towards uranium dioxide. In the presence of water vapor, there is very little U_3O_8 or $\text{UO}_{2.X}$ compound formation [Ritchie (1981)]. The extent of this effect is directly proportional to the partial pressure of the water vapor and oxygen. As the plume disperses, the boundary of the plume will see both an increase in the relative amount of oxygen and water vapor. During the decay period of the fire, when temperatures drop back into the UO_2 stability range, the particulate may consist of a different oxidation state than that during the incipient stage of the event. The latter particulate, UO_2 , is more susceptible to the induced dipole moment from the water vapor and subsequent scrubbing effect [Ritchie (1981)]. This is a form of wet deposition affecting the dispersion.

When taken as a form of wet deposition, the formation of hydrates and the scrubbing effect can significantly reduce the concentration of the uranium aerosol [Condon et al (1983) and Ritchie (1981)]. However, since these impacts only increase the dispersion, they are typically not considered in consequence modeling in order to ensure a reasonably conservative bounding consequence estimate is generated. When taken into account with Gaussian dispersion, the impact of wet deposition reduces the relative concentration to less than 10% (~ 2%) of the value for no deposition at 100 m from the source. Because of the order of magnitude impacts wet deposition can have on the aerosol concentration, and the general volatility of the wet deposition variables, wet deposition is not allowable under regulatory guidelines when determining the worst case consequences from the release of uranium aerosol.

5.5. Summary of Dispersion Impact When Determining Initial Oxide Fume

The general impacts during the dispersion of the oxide fume are that only the quasi-stable aerosol is subject to Gaussian dispersion. At distances greater than 100 meters, the suspended particulate in the oxide fume will settle until the aerosol entrainment is particulate $< 30 \mu\text{m D}_{\text{AE}}$. Limiting the airborne release fraction to the aerosol has no impact on determining consequences to human beings since the largest respirable particle is between $7 \mu\text{m}$ and $10 \mu\text{m D}_{\text{AE}}$. When determining the potential consequences to the environment, distances less than 100 meters are not of concern since they are a prerequisite inclusion in post-event clean-up actions. This distance is more than sufficient for particulate $> 20 \mu\text{m D}_{\text{AE}}$ to settle out of suspension depending on local wind velocities and atmospheric stability. Effects on the dispersion such as dry deposition and wet deposition apply primarily to the stable or quasi-stable aerosol and not the entire particulate. Consequently, the release fraction determining the source input to the Gaussian dispersion should be based solely on the aerosol and not the entire oxide fume.

CHAPTER 6 - Application of Release Fractions

The application of release fractions is used to quantify the portion of uranium that oxidizes and becomes aerosol. Therefore the maximum particulate size that should be taken into consideration is $30 \mu\text{m } D_{\text{AE}}$. The distribution of particulate size is dependent on the specific area of the uranium piece and the thermal stress to which that piece is exposed [ANSI (1998)]. In order to provide guidance to analysts when determining potential consequences in their nuclear facilities, the Department of Energy developed a handbook on Airborne Release Fractions and Respirable Fractions, DOE-HDBK-3010 [DOE (1994)]. This handbook contains many materials of concern and various stresses that can be imparted on these materials and forms.

The principal interest is the review of experiments that led to the bounding release fraction determination for uranium undergoing thermal stress at temperatures below the melting point. Numerous experiments are discussed in the handbook. However, there are two sets of experiments of principal interest for the uranium metal forms discussed herein that provide the bounding empirical release fractions. Using the arguments presented in this work, the bounding values will be revisited using specific area as a point of reference. Recommendations will be made to include in the handbook more appropriate bounding and median release fractions.

6.1. Review of the Experiments and Conclusions of DOE-HDBK-3010-94

DOE-HDBK-3010 [DOE (1994)] defines a pair of release fractions, the Airborne Release Fraction (ARF) and Respirable Fraction (RF) that are used together with the total release fraction taken as $\text{ARF} \times \text{RF}$. The Airborne Release Fraction is intended to be the entire aerosol that is released from the source and the Respirable Fraction is the portion of that aerosol $< 10 \mu\text{m } D_{\text{AE}}$. Generally for uranium the ARF applies to the quasi-stable aerosol and the RF is set to 1.0 indicating the aerosol is taken as fully stable. The handbook [DOE (1994)] describes many series of experiments performed on depleted uranium rods used as penetrators in armor-defeating weapons. These experiments provide the best match of available data to the conditions expected in fires that involve bulk forms of uranium.

In a specific series of tests performed on the XM774 [Elder and Tinkle (1980)], the rods were heated in a rack in an upflow of air. In the first three tests, the heat was generated from either ignited uranium turnings or munitions propellant. In the fourth test, heat was supplied by 10 batches of wood and paper packing materials. In twelve of the tests, a gas velocity of 2.23 m/s (5 mph) was passed around the oxidizing rod. In one experiment (air at 700°C), the test was performed with no gas flow. The penetrators were simultaneously exposed to fires fueled by uranium turnings, munitions propellant, or wood and paper packing materials and to flowing gases, either air or a mixture of 50% air and 50% CO₂. The gas temperature was controlled at steps between 500 and 1000°C. The burn periods were either two or four hours. No self-sustained reaction was observed under any of the test conditions. This leads to the conclusion that an external heat source is required to sustain uranium combustion for the size of the uranium penetrators used in the experiments.

DOE-HDBK-3010 [DOE (1994)] also describes a series of experiments performed by Carter and Stewart (1970) on uranium metal turnings. These experiments provide the best match of available data to the conditions expected in fires that involve uranium chips, fines, or any piece of uranium with a large specific area. These tests were conducted using free-falling uranium metal turnings in a countercurrent air flow chamber.

The experiments included in DOE-HDBK-3010 look at a variety of fire scenarios from extremely energetic munitions fires to small thermal events limited to typical packing materials. In the majority of cases, the airborne release fraction was determined based on the airborne particulate < 10 μm D_{AE} collected on filter media. There is general agreement between the values except for one outlying case which the authors used to postulate the bounding ARF value. The outlying case is an extrapolation from suspect filter data. In comparison, the general reference case that appears to bound the majority of the work done on depleted uranium penetrators is the Carter and Stewart (1970) experiments. The outlying case is the experiment by Elder and Tinkle (1980) using 10 batches of combustible fuel. A review of both cases against the arguments previously presented outlines the disparity and potential causes thereof. Where applicable the difference between the quasi-stable aerosol and fully stable aerosol will be inferred based on the experimental results and measurement techniques.

6.2. Analysis of the Bounding ARF/RF Values From Carter and Stewart

The results of the Carter and Stewart Experiments bound the estimated $ARF \times RF$ value for pieces of uranium that reach complete oxidation such as chips, fines, or small pieces of metal with large specific areas or substantially long burn times [Carter and Stewart (1970)]. Uranium metal turnings ($9 \text{ cm}^2/\text{g}$) were allowed to burn in a free fall in a column with countercurrent air flow. Various column heights ranging from 0.2 m to 3.5 m were used and an additional series was performed using sieved fraction of silica sand dispersed at the moment of aerosol formation to determine the efficiency of removal of the aerosol by inert particles. The results of these tests are shown in Table 6.1.

Table 6.1 Results From Carter and Stewart (1970) Experiments

	Fraction of source released as aerosol $< 10 \mu\text{m}$ unit density	
	Plutonium	Uranium
Ignition and Burning in Air	7×10^{-6} (a)	1.1×10^{-4} (a)
	1×10^{-4} (b)	3.6×10^{-4} (b)
Melting	7×10^{-6} (a)	(1)
	1×10^{-4} (b)	
Partial Disruption of liquid into droplets (2)	3.5×10^{-3} (a)	1.9×10^{-3} (a)
	1×10^{-2} (b)	6×10^{-3} (b)
Vapor formation from droplets	About 0.5	

Notes: (a) Geometric Mean (b) 95% confidence limit

(1) Massive Uranium does not melt after ignition unless there is an external heat supply.

Heat losses cause self-extinguishing unless some form of insulation (oxide) is present.

(2) Height of fall approximately 0.75 m

These values allow for entrained fines with oxide and the turbulent flow conditions exposed the entire surface area of the turnings for oxidation which is not a representative condition of a metal fire involving an open pile or material in a stainless steel canister. These forms of uranium were taken past the ignition point as shown on Figure 4.1 which leads to the generation of finer particulate as the general reaction is direct oxidation opposed to diffusion dominated oxidation. Carter and Stewart (1970) noted that "...the results indicated that the quantity of airborne

particulate created by a fall of 4 m was about 50 times greater than that produced by static oxidation” which is reflected in the upper confidence value of 3.6×10^{-4} .

In general application this upper confidence limit bounds the response of uranium materials at points above their ignition temperature, which for most uranium forms and potential fire scenarios would apply to all materials with specific areas greater than $1 \text{ cm}^2/\text{g}$. The geometric mean showed close agreement with the upper confidence value and is more appropriate for local velocities of 1 m/s. Whereby the upper confidence values takes into account the effects of velocities that would entrain material into the quasi-stable aerosol, the geometric mean value is a bounding approximation of the stable aerosol. The general order of magnitude of both values for ARF x RF of 10^{-4} is in close agreement with the other tests in DOE-HDBK-3010.

6.3. Analysis of the Maximum ARF/RF Values From Elder and Tinkle

The bounding value as presented in DOE-HDBK-3010 [DOE (1994)] is based on a conservative response to an outlying data point from the outdoor burn test #4 performed by Elder and Tinkle on β -stabilized Staballoy depleted uranium penetrators [Elder and Tinkle (1980)]. The outdoor burn test refueled the combustion chamber 10 times with a fuel to uranium mass ratio of 2.5:1 to achieve a total burn duration of 3 hours. The mass of the airborne depleted uranium was collected by high-volume air samplers with flow rates up to $0.038 \text{ m}^3/\text{s}$ (50 cfm) that were used to determine airborne mass concentrations. The mass of the airborne material collected was determined by γ -counting $\frac{1}{4}$ of the surface area of the filter and extrapolating the data. For quantities $<0.040 \text{ mg}$, portions of the filters were acid leached with hydrochloric acid and ion-exchanged for the removal of sodium (with $\sim 40\%$ recovery), and the mass determined by delayed neutron counting with a lower detection limit of $0.02 \text{ }\mu\text{g}$ uranium mass.

Most of the particle size information was obtained using one of two configurations of an inertial cascade impactor. The short impactor configuration provided dAED >10 and $<10 \text{ }\mu\text{m}$ information with fewer intermediate samples. The impactor mass data was analyzed by computer using a least-squares curve fitting that assumed a log normal distribution of particle aerodynamic diameters. The distribution is described by two parameters—Mass Median Aerodynamic Diameter (MMAD) and geometric standard deviation (σG). The data included only stage masses;

it did not consider the pre-cutter mass due to the predominance of this mass. Including the pre-cutter as a stage resulted in MMAD >20 μm which would indicate the agglomeration of larger mass from the oxide fume and not a fully developed stable or quasi-stable aerosol. The mass of the pre-cutter and zero-stage was reported separately due to the sporadic temperatures in the apparatus and variable sampling durations.

The measurement equipment used in these analyses did not correct for temperature effects on the filter media and flow rates. The maximum error in D50 (largest cascade impactor stage cutoff at the pre-cutter and stage-0) is proportional to viscosity of air that increases from 183 μp at 18°C to 211 μp at 75°C. The maximum error for the pre-cutter and first few stages was ~ 1.07 or <10%. This indicates that approximately 7% of the mass that was reported as part of the aerosol in equilibrium past the pre-cutter was actually portions of the unstable oxide fume that should have been excluded from the sample.

The sampling flow rate for both the 47-mm filter and the cascade impactor is 28-L/min, shown in Table 6.2 and is extracted isokinetically. The flow through the apparatus was nominally 225 cm/s, giving fully developed turbulent flow based on the inside diameter of 15 cm. The cross-sectional area of the apparatus is $A = 0.7854[15 \text{ cm}]^2 = 176.715 \text{ cm}^2$. The flow through the duct is $225 \text{ cm/s} \times 176.715 \text{ cm}^2 = 39,760.875 \text{ cm}^3/\text{s}$ or 2385.65 L/min (84.24 cfm). The total weight of the three penetrators within the apparatus is: $3[3355 \text{ g}] = 10,065 \text{ g}$.

Based on the data cited in Table 6.2, the mass concentration indicated by the 47-mm filter samples and a sampling rate of 28 L/min, the airborne mass can be estimated as follows:

$$0.932 \text{ mg} \cdot 2389 \text{ L/min} \div 28 \text{ L/min} = 79.5 \text{ mg};$$

$$15.062 \text{ mg} \cdot 2389 \text{ L/min} \div 28 \text{ L/min} = 1285 \text{ mg};$$

$$109.407 \text{ mg} \cdot 2389 \text{ L/min} \div 28 \text{ L/min} = 9335 \text{ mg}; \text{ and}$$

$$45.794 \text{ mg} \cdot 2389 \text{ L/min} \div 28 \text{ L/min} = 3907 \text{ mg}.$$

Table 6.2 Elder and Tinkle (1980) Outdoor Burn Test # 4 Air Sampling Data

Sample	Batch 1	Batch 4	Batch 8	Batch 10
47-mm filter, gross wt., µg	931	15,062	109,407	45,794
Andersen Cascade Impactor				
Pre-cutter, µg	482	5,695	13,998	14,980
Stage 0, µg	[a]	1042 ^[b]	[a]	[a]
Stage 1, µg	[a]	58 ^[b]	[a]	[a]
Stage 2, µg	[a]	34 ^[b]	[a]	[a]
Stage 3, µg	[a]	9.8 ^[b]	[a]	[a]
Stage 4, µg	[a]	13.5 ^[b]	[a]	[a]
Stage 5, µg	[a]	4.5 ^[b]	[a]	[a]
Stage 6, µg	[a]	5.9 ^[b]	[a]	[a]
Stage 7, µg	[a]	5.4 ^[b]	[a]	[a]
Backup filter, µg	489	270	21,995	24,408
Impactor total, µg ^[c]	971	7138	35,993	39,388
Percent <d _{AED} 10-µm ^[d]	50	20	61	62
Sampling time, min ^[e]	8	5	5	5
Sampling rate, L/min	28	28	28	28
Duct DU Mass Conc, mg/m ³ [f]	4.2	108	782	327

^[a] Sample not taken, short impactor used.

^[b] Particle size characteristics could not be analyzed from these data due to preponderance of mass on Stage 0. [Indicates that airborne material predominantly (94.4%) >9 µm.]

^[c] Includes mass collected on pre-cutter.

^[d] Percent <10 µm – [(Impactor Total – Pre-cutter) ÷ Impactor Total] × 100.

^[e] Same sampling rate for cascade impactor and gross sampler.

^[f] Calculated from gross 47-mm sampler mass. Mass concentration based on the sum of nine masses on impactor stage is not considered as reliable as a single mass on the gross filter.

Based on the initial total mass of the penetrators, the ARF values for these periods are as follows:

$$\begin{aligned}
 0.0795 \text{ g} \div 10,065 \text{ g} &= \text{ARF } 7.9\text{E-}6, \text{ RF } 0.50; & \text{ARF} \times \text{RF} &= 4.0\text{E-}6 \\
 1.285 \text{ g} \div 10,065 \text{ g} &= \text{ARF } 1.3\text{E-}4, \text{ RF } 0.28; & \text{ARF} \times \text{RF} &= 3.6\text{E-}5 \\
 9.335 \text{ g} \div 10,065 \text{ g} &= \text{ARF } 9.3\text{E-}4, \text{ RF } 0.61; & \text{ARF} \times \text{RF} &= 5.7\text{E-}4 \text{ and} \\
 3.907 \text{ g} \div 10,065 \text{ g} &= \text{ARF } 3.9\text{E-}4, \text{ RF } 0.62. & \text{ARF} \times \text{RF} &= 2.4\text{E-}4
 \end{aligned}$$

The overall ARF value cannot be deduced due to the lack of knowledge of the relative importance of the separate values and to the lack of data on the remaining ARF values for the six other sampling periods. The average ARF value of the data is 3.6E-4 which coincidentally is the upper confidence level for the Carter and Stewart (1970) experiments without taking into account the effects of RF. The average for the RF values calculated based on the suspect cascade impactor data is 0.5. To determine the quasi-stable aerosol, the ARF values must be multiplied by the maximum RF. Taking this into account brings all except for the Batch 8 into agreement with the Carter and Stewart upper confidence level.

The oxide mass concentrations of effluent from the downstream end of the apparatus were measured after each batch of fuel had actively rekindled (4 to 5 minutes after restart of blower). Variations in the mass concentrations were attributed to temperature cycling and differential thermal expansion of base metal. Sampling was performed during periods of maximum material dispersal, specifically when the oxide fume was at maximum concentration irrespective of the aerosol stability. Although high mass concentrations should have been visually apparent indicating that the oxide fume was not a stable aerosol, a visible plume was only observed during blower restart when sampling was not performed. This indicates that the additional mass on the Batch 8 gross 47-mm filter collected larger particulate suspended temporarily in the oxide fume.

The weight percent for particles $d_{AED} < 10 \mu\text{m}$ ranged from 28 to 62% indicating a high fraction of the particles in the respirable size range, as would be expected with the quasi-stable aerosol. The low value, 28 wt%, is suspect with respect to other samples, although this is the only set of data where a full cascade impactor was used and no instrument clogging was observed. All of these indications are that the separation distance of 3 meters was insufficient for the aerosol to separate from the oxide fume thus increasing the resultant apparent release fraction.

For most facility fires, the fire will initially grow to a maximum intensity and then diminish in intensity as the fuel is consumed. Combustible material that is ignited by the fire would be expected to burn until either the fire is extinguished or the fuel is consumed. As the fire burns down and cools, there would be a lower initial velocity of the fire plume and a decreased capacity to entrain uranium combustion products. If the fire involves significant amounts of combustible materials such as wood that could smolder at relatively low temperatures, during the smoldering phase the uranium would either be released at a relatively low rate or, more likely, the uranium fire would self extinguish with no significant additional oxidation. The refueling of the fire cycled the material through each of these phases numerous times leading to larger disparities between the oxide fume and aerosol.

The ARF of $5.7\text{E-}4$ with RF of 0.61 was used as the reference point whereby the authors of DOE-HDBK-3010 [DOE (1994)] chose to specify a bounding ARF of $1\text{E-}3$ with RF of 1.0 to conservatively cover any possible thermal stress scenarios involving uranium that could generate

airborne particulate. The bounding ARF/RF value of 1E-3/1.0 is not based on data and is arbitrarily extrapolated from the Batch 8 sample of the Elder and Tinkle outdoor burn test # 4. The total release fraction ARF \times RF of 5.7E-04 appears to be based on a pre-filter mass not indicative of a stable aerosol.

6.4. Analysis of the Primary ARF/RF Values From Elder and Tinkle

The controlled temperature experiments by Elder and Tinkle report maximum release fractions (ARF \times RF) for 9 experiments on the XM774 penetrator that are directly comparable to the other depleted uranium experiments [Elder and Tinkle (1980)]. The data from the other experiments was not obtained. The maximum ARF for uranium based on the controlled temperature experiments shown in Tables 3.2 and 3.3, (where bulk uranium forms are below the ignition temperature), is an order of magnitude less than the average ARF for ignitable uranium forms. The summary of the ARFs and RFs shown in Table 6.3 is based solely on the amount of oxidized material and not the mass of the initial piece, isolating damage ratios. The Release Fraction (ARF \times RF) is the point of reference for quantifying stable and quasi-stable aerosols.

Table 6.3 Summary of Controlled Temperature Experiments by Elder and Tinkle (1980)

	Airborne Release Fraction (ARF)	Respirable Fraction (RF)	Airborne Respirable Release Fraction (ARF \times RF)
500 °C Air	3.2E-05	0.04545	1.5E-06
600 °C Air	2.6E-05	0.10625	2.7E-06
700 °C Air	8.6E-05	0.03000	2.6E-06
800 °C Air	5.1E-05	0.04111	2.1E-06
900 °C Air	2.1E-04	0.11515	2.4E-05
600 °C Air + CO ₂	7.1E-05	0.05556	4.0E-06
700 °C Air + CO ₂	2.7E-04	0.14655	4.0E-05
800 °C Air + CO ₂	5.0E-05	0.01533	7.6E-07
1000 °C Air + CO ₂	4.7E-04	0.07182	3.3E-05
Arithmetic Mean			1.2E-05
Geometric Mean			5.0E-06
<i>Omitting the 1000 °C Air + CO₂ run due to the formation of molten uranium metal droplets</i>			
Arithmetic Mean			9.7E-06
Geometric Mean			4.0E-06

The 1000 °C experiment in the Air-CO₂ mixture experiences localized temperature fluctuations like those shown in Figure 4.1 except that upper limit is the melting point which plateaus the peaks leading to moderated temperature fluctuations as the surface becomes molten. Due to molten uranium having different aerosol characteristics, and the preponderance of liquefaction, the 1000 °C data can be omitted and a more characteristic average of the release fraction is obtained for thermal stress on uranium below the melting point.

6.5. Recommendations of ARF/RF Values Based on Specific Area

The specific area of 1 cm²/g emerges as dividing line for characterizing uranium into two forms; ignitable and non-ignitable. Ignitable forms of uranium metal will generate an aerosol that is finely divided in form with an ARF and RF that is bounded by the Carter and Stewart experiments. Non-ignitable forms of uranium metal generate less aerosol based on the reaction kinetics and are similar to the Elder and Tinkle controlled temperature experiments.

The geometric mean value from the Carter and Stewart experiments with an ARF = 1.1E-4 and RF = 1.0 incorporate conditions that conservatively bound the formation of stable aerosol and incorporate a large portion of the quasi-stable aerosol. When determining the source term subject to Gaussian plume dispersion at distance greater than 100 meters, the generalized release fraction of 1.1E-4 (ARF_xRF) should be used for all uranium forms with specific areas greater than 1.0 cm²/g.

The controlled temperature experiments by Elder and Tinkle (1980) report maximum release fractions (ARF_xRF) for 11 experiments on the XM774 penetrator that are directly comparable to the other depleted uranium experiments. The maximum ARF for uranium based on the controlled temperatures shown in Tables 3.2 and 3.3, (where bulk uranium forms are below the ignition temperature), is an order of magnitude less than the average ARF for ignitable uranium forms. The entrainment velocities and particle size distributions necessary to form a stable aerosol indicate that the geometric mean value from the Elder and Tinkle controlled temperature experiments with a nominalized ARF = 1.0E-5 / RF = 1.0 are appropriate for uranium forms with specific areas less than 1.0 cm²/g.

This page intentionally left blank.

CHAPTER 7 - Conclusions Regarding Uranium Release Fractions

The motto “Hope for the best, but prepare for the worst” summarizes the field of consequence analysis where analysts try to quantify potential consequences from a myriad of different scenarios. For facilities with large quantities of metals, the main source of concern is the response to thermal stress induced by a fire. The general postulation of consequences from a fire is very subjective if adequate technical guidance does not exist. Therefore to aid in these determinations, the Department of Energy set out to prepare a handbook of technical guidance for release fractions in DOE-HDBK-3010 [DOE (1994)].

The preparation of DOE-HDBK-3010 summarized 30 years of data from various tests that contained information on airborne particulate and size distributions of that particulate for numerous types of materials of concern. The schedule and scope of the development of the handbook minimized the time available for critical review of apparent disparities in the available data. Subsequently various levels of conservativeness were built into the initial issuance of the handbook. More hazardous compounds, like plutonium, were given critical review to determine a singular release fraction recommendation compared to less hazardous materials, like uranium, that were given a median and bounding release fraction to allow the analyst to perform the critical review as necessary. This work summarizes the critical review of a singular condition in the handbook, the release fraction from the thermal stress of uranium below the melting point.

7.1. Recommendations for the Revision of DOE-HDBK-3010

Significant additional conservativeness was included in the bounding release fraction for uranium under thermal stress. Looking at how uranium reacts to thermal oxidation, specifically the crystalline structure change, reaction kinetics, and selectivity provides a basis to determine the characteristics of the oxide fume and aerosol. The overall qualification of the oxide fume and aerosol is somewhat dependent on the thermal stress imparted, but postulated fire scenarios in this work and actual fires used in various experiments show the primary relationship is in reference to the ignition temperature of the material. This behavior allows uranium shapes to be separated into ignitable and non-ignitable categories based on the specific area.

Uranium above the ignition point is dominated by direct oxidation and the material generates a fine particulate where the entrainment is proportional to the gas velocity. The fine particulate ($< 30 \mu\text{m } D_{AE}$) generated above the ignition point minimizes the disparity between the oxide fume and the aerosol. This generates a quasi-stable aerosol that at general atmospheric velocities (i.e. F-stability, 1 m/s) has an upper-confidence-level release fraction of $ARF \times RF = 1.1E-4$.

Uranium below the ignition point is dominated by oxygen diffusion through the porous oxide layers generating a more adherent particulate of relatively large size (e.g. $100 \mu\text{m}$) in addition to the fine particulate [Stakebake (1979)]. This disparity in the nominal size of particulates generates a significant disparity between the initial oxide fume and the quasi-stable aerosol. The unstable portions of the oxide fume are rarely transported more than 5 meters and therefore should be excluded from dispersion calculations that consider transport in excess of that distance. The quasi-stable aerosol for uranium oxidizing below the ignition temperature and below the melting temperature has a nominal release fraction of $ARF \times RF = 9.7E-6$. The geometric deviation is approximately half this value and the normal particulate size distribution indicates that this value includes portions of the oxide fume above the quasi-stable aerosol state. Therefore a release fraction of $1E-5$ is recommended for uranium below the ignition point.

Using specific area in relationship to the ignition point and uranium forms discussed in this work leads to a pair of release fraction recommendations. Uranium metal forms discussed in Section 2.1.1 are non-pyrophoric and have specific areas much less than $1 \text{ cm}^2/\text{g}$. Uranium chips, fines, and turnings discussed in Section 2.1.2 are generally pyrophoric and have specific areas greater than $1 \text{ cm}^2/\text{g}$. Since pyrophoricity is generally easier for individuals to understand than specific area and the handbook is for general use, the terms pyrophoric and non-pyrophoric forms are recommended as opposed to ignitable and non-ignitable. Therefore the recommendation for revision of the portion of DOE-HDBK-3010 dealing with thermal stress of uranium below the melting point is:

PYROPHORIC FORMS	$ARF / RF = 1E-4 / 1.0$
NON-PYROPHORIC FORMS	$ARF / RF = 1E-5 / 1.0$

7.2. Considerations for Future Testing.

Additional testing on uranium forms can be performed to potentially lower the threshold for non-pyrophoric forms. The relationship between the oxide fume and the aerosol is of principal interest and more data is needed on the distance required for separation. Based on munitions tests and debris field distribution of particulate size, indications are that the sample filter media has been located in the oxide fume and not measuring quasi-stable or stable aerosol. An understanding and accommodation for effective length is necessary when trying to determine the source term that will be subject to atmospheric dispersion.

When sampling for airborne particulate the effects of velocity, temperature, and distance from the source need to be taken into account. Lessons learned are that the measurement devices need to be calibrated to the temperatures of the sampling. Other considerations to be taken into account are that the face velocity on the uranium piece can be set at a nominal rate, but the effective velocity between the piece and the sampling location also needs to be considered. Many apparatus configurations decreased the diameter of the pipe between the uranium chamber and the sample location, increasing velocity in fully developed turbulent flow that lead to a shift of the aerosol into quasi-stability with larger entrained particulate. This effect can significantly increase the mass on the pre-cutter and skew the release fraction determination. The last consideration, temperature is much more difficult since temperatures below 100 °C lead to the accumulation of the water droplets clogging the filter and beginning to strip airborne particulate. Ideally the temperature at the sample location needs to be less than 190 °C to allow the UO₂ end state to stabilize and not continue a shift to U₃O₈ if not already thus oxidized.

An understanding of the crystalline structure progression and the density fluctuations with temperature indicate that experiments which could monitor the structure changes could serve as the necessary bridge to understand how the atomistic scale interactions initiate the mesoscale fluctuations causing the release of particulate. Any experiment that could monitor the framework as quickly as the progression occurs would provide invaluable insight into the determination of a microscale model of uranium oxidation. This microscale model is necessary to expand upon the Gibbs free energy models and generate an understanding of the transition stage and ignition characteristics of specific areas less than 1 cm²/g.

7.3. Closing Summary

Uranium is a versatile element that can form numerous compounds, but the oxides are generated under thermal stress and pose a health risk to human beings, primarily through inhalation. Uranium progresses through multiple crystalline structure transformations during the oxidation process. The reaction kinetics and selectivity as the oxidation progresses are based on specific area at temperatures above and below the ignition point. The oxide fume that is generated from the initial thermal event will separate over the first few meters into a quasi-stable aerosol that will stabilize based on the ambient conditions as the fume disperses. A critical review of the oxide fume shows that for uranium only the aerosol is subject to atmospheric dispersion. The quantification of the aerosol is therefore extracted from the available experiments on the oxide fume as a composite release fraction consisting of the Airborne Release Fraction (ARF) and Respirable Fraction (RF).

This review indicates that the recommended bounding value for the ARF and RF of uranium metal subject to thermal stress at temperatures below the melting point are at least an order of magnitude higher than the data and characteristic response of uranium oxidation support. This data is used to postulate consequences of events and determine risk mitigation techniques. In the interest of ensuring that derived controls are actually appropriate to reduce the risk of accidents involving the oxidation of uranium metal, the release fraction (ARFxRF) needs to reflect the chemical response of the material supported by experimental data. The recommendations are to lower the release fraction recommendation to the value currently supported by experimental data and confirm the stability of the uranium aerosol through carefully designed future experiments.

References

- Allen, G.C., and P.A. Tempest, January 1986. "Ordered Defects in the Oxides of Uranium," Mathematical and Physical Sciences (Proceedings of the Royal Society of London), 406 No. 1831:pp. 325–344.
- ANSI, 1998. American National Standard for Airborne Release Fractions at Non-Reactor Nuclear Facilities, ANSI/ANS-5.10-1998, American Nuclear Society, 1998
- Aronson, S., R.B. Roof, and J. Belle. 1957. "Kinetic Study of the Oxidation of Uranium Dioxide," Journal of Chemical Physics, 27(1):pp. 137–144.
- Baker, I. Jr., and J.D. Bingle. 1966a. "The Kinetics of Oxidation of Uranium between 300 and 625 °C," Journal of Nuclear Materials, 20:pp. 11–21.
- Baker, I. Jr., J.G. Schnizlein, and J.D. Bingle. 1966b. "The Ignition of Uranium," Journal of Nuclear Materials, 20:pp. 22–38.
- Belle, J. July 1961. Uranium Dioxide, Properties and Nuclear Applications, United States Atomic Energy Commission, Washington, DC.
- Bennett, M.J. and J.B. Price. 1981. "The Oxidation Behavior of Uranium in Air at 348 – 756 K," Journal of Nuclear Materials, 101:pp. 44–55.
- Bloch, J., U. Atzmony, M.P. Mintz, and N. Shamir. 1982. "Surface Spectroscopy Studies of the Oxidation Behavior of Uranium," Journal of Nuclear Materials, 105:pp. 196–200.
- Carter, R.F. and K. Stewart. 1970. "On the Oxide Fume Formed by the Combustion of Plutonium and Uranium", Inhaled Particles III (Proceedings of an International Symposium, British Occupational Hygiene Society, London, 9/14-23/70), Unwin Brothers Limited – The Gresham Press, Old Working, Surrey, England.
- Chambers, D.R., R.A. Markland, M.K. Clary and R.L. Bowman. October 1982. Aerosolization Characteristics of Hard Impact Testing of Depleted Uranium Penetrators, ARBRL-TR-02435, Ballistic Research Laboratory, Aberdeen Proving Grounds, MD 21005.
- Coleman, L.F and L.C. Schwendiman,, August 1962. Particles Generated During the Air Oxidation of Uranium, HW-SA-2641, Hanford Laboratory, Richland, WA 99352.
- Colmenares, C., R. Howell, and T. McCreary. 1981. Oxidation of Uranium Studied by Gravimetric and Positron Annihilation, URCL-85549, Lawrence Livermore National Laboratory, Livermore, CA.
- Condon, J.B., S.S. Cristy, and .. Kirkpatrick. 1983. Uranium Reaction with Water Vapor, V/DU-274, Oak Ridge Y-12 Plant, Oak Ridge, TN.
- Connors, E.W., and D.P. O'Neil, June 1954. Efficiency Studies of a High-Efficiency, High-Temperature Filter Against Freshly Generated Uranium Oxide Fume, ANL-5453, Argonne National Laboratory, Lemont, IL
- Cubicciotti, D. February 1952. "The Reaction between Uranium and Oxygen", Journal of the American Chemical Society, Volume 74, Page 1079.
- DOE. January 1976. Handbook on Aerosols, TID-26608, U.S. Department of Energy, Washington, DC.

- DOE. December 1994. DOE Handbook of Airborne Release Fractions/Rates and Respirable Fractions for Nonreactor Nuclear Facilities Volume I - Analysis of Experimental Data, DOE-HDBK-3010-94, U.S. Department of Energy, Washington, DC.
- Dungan, K.W. December 2003. Lift Truck Fire Calculation, DAC-FPD-972082-A003, Oak Ridge, TN
- Elder, J.C. and M.C. Tinkle. December 1980. Oxidation of Depleted Uranium Penetrators and Aerosol Dispersal at High Temperatures, LA-8610-MS, Los Alamos National Laboratory, Los Alamos, NM 87545.
- Gittus, J.N. 1963. Ch 12 “Gaseous and Aqueous Corrosion,” Uranium, Butterworth’s, Washington, D.C.
- Glassner, A. January 1957. The Thermochemical Properties of the Oxides, Fluorides, and Chlorides to 2500 K, ANL-5750, Argonne National Laboratory, Lemont, IL
- Glissmeyer, G.A. and J. Mishima. November 1979. Characterization of Airborne Uranium From Test Firings of XM774 Ammunition, PNL-2944, Pacific Northwest Laboratory, Richland, WA 99352.
- Green, D.W. (ed), 2008. Perry’s Chemical Engineers’ Handbook, 8th Ed., McGraw-Hill, New York, NY.
- Grenthe, I. et al, 2004. Chemical Thermodynamics Of Uranium, Nuclear Energy Agency, Organisation for Economic Co-Operation and Development, Paris, France.
- Guéneau, C., M. Baichi, D. Labroche, C. Chatillon, and B. Sundman. May 2002. “Thermodynamic Assessment of the Uranium-Oxygen System”, Journal of Nuclear Materials, 304:pp. 161-175.
- Hanna, S.R., G.A. Briggs, and R.P. Hosker, December 1982. Handbook on Atmospheric Diffusion, DOE/TIC-11223, U.S. Department of Energy, Washington, DC
- Hanson, W.C., J.C. Elder, H.J. Ettinger, L.W. Hantel and J.W. Owens. October 1974. Particle Size Distribution of Fragments from Depleted Uranium Penetrators Fired Against Armor Plate Targets, LA-5654, Los Alamos National Laboratory, Los Alamos, NM 87544.
- Harrington, C.D. and A.E. Ruehle. 1959. Uranium Production Technology, D. Van Nostrand Company, Inc., New York, N.Y.
- Hilliard, R.K. 1958. Oxidation of Uranium at High Temperatures, HW-58022, HAPO-General Electric, Richland, Wash.
- Iqbal, N., and M.H. Salley. December 2004. Fire Dynamics Tools (FDTs) Quantitative Fire Hazard Analysis Methods for the U.S. Nuclear Regulatory Commission Fire Protection Inspection Program, (NUREG-1805), U.S. Nuclear Regulatory Commission Office of Nuclear Reactor Regulation Division of System Safety and Analysis, Washington, DC.
- Isaacs, J. W. and Wanklyn, J. N. December 1960, The Reaction of Uranium with Air at High Temperatures, AERE-R 3559, Atomic Energy Research Group, United Kingdom
- Iwasaki, I. and N. Nishikawa. 1970. “Air Oxidation of UO₂ Pellets at 800° and 900°C,” Journal of Nuclear Materials, 36:pp. 116–119.
- Iwasaki, M, T. Sukurai, N. Ishikawa, and Y. Kobayashi. 1969. Oxidative Pulverization of UO₂ Pellets, JAERI-1171, Japan Atomic Energy Institute, Japan.
- Jackson, R.L., J.B. Gordon, and L.M. Steckle. 1977. Uranium/Water Vapor Reactions in Gaseous Atmospheres, Y-2078, Oak Ridge, TN.
- Jette, S.J., J.A. Glissmeyer, J. Mishima, D.J. Sherwood and R.E. Williford. August 1989. Potential Aerosolization (Airborne Suspension) of Depleted Uranium During Test Firings, PNL-7137 Informal Letter Report, Pacific Northwest Laboratory, Richland, WA 99352.

- Jette, S.J., J. Mishima and D.E. Hadlock. August 1990. Aerosolization of the M829A1 and XM900E1 Rounds Fired Against Hard Targets, PNL-7452, Pacific Northwest Laboratory, Richland, WA 99352.
- Katz, J. J., and E. I. Rabinowitch, August 1951. The Chemistry of Uranium, McGraw-Hill, New York, NY
- Klein, J.L. 1962. Chapter 3 – “Uranium and Its Alloys”, Nuclear Reactor Fuel Elements (Kaufman, A.R., Ed), Interscience Publishers – John Wiley and Sons, New York, N.Y.
- Leibowitz, L., J.G. Schnizlein, J.D. Bingle, and R.C. Vogel. 1961. “The Kinetics of Oxidation of Uranium Between 125° and 250°C,” Journal of the Electrochemical Society, 108:No. 12, pp. 1155–1160.
- McEachern, R.J., and P. Taylor, January 1997. A Review of the Oxidation of Uranium Dioxide at Temperatures Below 400 °C, AECL-1135, Whiteshell Laboratories, Pinawa, Manitoba, Canada
- McGuire, S., January 1988. Regulatory Analysis on Emergency Preparedness for Fuel Cycle and Other Radioactive Material Licensees, (NUREG-1140), U.S. Nuclear Regulatory Commission Office of Nuclear Reactor Regulation Division of System Safety and Analysis, Washington, DC.
- Megaw, W.J., R.C. Chadwick, A.C. Wells, and J.E. Bridges. December 1961. “The Oxidation and Release of Iodine-131 from Uranium Slugs Oxidizing in Air and Carbon Dioxide”, Journal of Nuclear Energy Parts A and B, Reactor Science and Technology, Volume 15, Atomic Energy Research Establishment, Harwell, Berks, England.
- Mishima, J., M.A. Parkhurst, R.I. Scherpelz and D.E. Hadlock. March 1985. Potential Behavior of Depleted Uranium Penetrators under Shipping and Bulk Storage Accident Conditions, PNL-5415, Pacific Northwest Laboratory, Richland, WA 99352.
- NIST, April 1995. Fire Protection Engineering Tool, FPEtool version 3.2, National Institute of Science and Technology, Building and Fire Research Laboratory, Gaithersburg, MD
- Parkhurst, M.A., J.A. Gissmeyer, <H. Smith, D.L. Haggard, K.M. Krupka, E.D. Jensen, B.W. Arey, C.Z. Sonderquist, and R.J. Traub. June 2004. Burn Test of M829A3 Cartridges in PA171 Containers, PNNL-14496, Pacific Northwest National Laboratory, Richland, Wash.
- Peakill, K.A. and J.E. Antill. 1960. “Oxidation of Uranium Dioxide in Air at 350° – 1000° C,” Journal of Nuclear Materials, 2:pp. 194–195.
- Peligot, M.E, May 1842. “Recherches sur l'Uranium,” Annales de Chimie et de Physique, 3rd Series, 5th Volume: pp. 5-47.
- Pizzolato, P.J et al. July 1957. Chemical Engineering Division Summary Report for January, February, and March 1957, Section III, Part A.1, ANL-5730, Argonne National Laboratory, Lemont, IL
- Ritchie, A.G. 1981. “A Review of the Rate of Uranium Oxidation with Oxygen and Water Vapor,” Journal of Nuclear Materials, 102:pp 170–182.
- SAIC. 1998. Nuclear Fuel Cycle Facility Accident Analysis Handbook, NUREG/CR-6410, Science Applications International Corporation, Reston, Va.
- Schnizlein, J.G., P.J. Pizzolato, H.A. Porte, J.D. Bingle, D.F. Fischer, L.W. Mishler, and R.C. Vogel. 1959. Ignition Behavior and Kinetics of Oxidation of Reactor Materials, ANL-5974, Argonne National Laboratory, Argonne, Ill.
- Schnizlein, J.G., L. Baker, Jr., and J.D. Bingle. 1966. “The Ignition of Binary Alloys of Uranium,” Journal of Nuclear Materials, 20:pp 39–47.

- Stakebake, J.L. 1979. Kinetics for the Reaction of Hydrogen with Uranium Powder, RFP-2845, Atomic International-Rocky Flats Plant, Golden, Colo.
- Steciak, J, A. Tewarson, and J.S. Newman. February 1983. Fire Properties of Combustible Materials Commonly Found in Nuclear Fuel Cycle Facilities, FMRC J.I OG3R8.RC, Factory Mutual Research, Norwood, Miss.
- Stinton, D.P., S.M. Tiegs, W.J. Lackey, and T.B. Lindmer. December 1979. “Rate Controlling Factors in the Carbothermic Preparation of UO₂-UC₂-C Microspheres,” J American Chemical Society, 6:11/12 pp. 596–599.
- Stobbs, J.J. and I. Whittle. 1966. “The Influence of Impurities on the Oxidation of Uranium in Carbon Dioxide Between 450° and 650°C,” Journal of Nuclear Materials, 19:pp. 160–168.
- Suzuki, Y., Y. Arai, T. Sasayama, and H. Watanabi. March 1962. “Kinetic on Carbothermic Reduction of UO₂ + C Powders in Compacts of UC₂,” Journal of Nuclear Science and Technology, 19:3, pp. 220–230.
- Tisch Environmental, Inc. November 2006. Instruction Manual, 8-Stage Non-Viable Cascade Impactor, Tisch Environmental, Inc., Cleves, OH.
- Tyzak, C. and H.C. Cowan. 1976. “Corrosion of Reactor Materials in Carbon Dioxide,” Atomic Energy Review, 142:pp. 263–324.
- Wakelin, R.J. September 1970. The Influence of Impurities on the Properties of Uranium, AWRE 0 63/70, Atomic Weapons Research Establishment, Aldermaston, Berkshire, England.
- Wang, X., F. Yibei, X. Renshou, and H. Riuliang December 1996. “Influence of Carbon Monoxide to the Surface Layer of Uranium Metal and Its Oxides”, CNIC-01102, Chinese Science and Nuclear Technology Report, Volume 28, Number 09, China Nuclear Information Centre Atomic Energy Press, Southwest Institute of Physics and Chemistry, Chengdu, China.
- Watts, B.N. and M.A. Cayless, January 1961. Treatment of Uranium, Patent GB 858656, British Thomson-Houston Co., Ltd, Rugby, Warwickshire, United Kingdom
- Wilkinson, W. D., December 1962. Uranium Metallurgy Volume I and II: Uranium Process Metallurgy, Uranium Corrosion and Alloys, Interscience Publishers, New York, NY

Appendix A - Physical Properties of Uranium

This appendix contains general properties of uranium metal as extracted from various sources.

A.1 Mechanical Properties of Uranium Metal

Table A.1 Mechanical Properties of Pure Uranium Metal [Klein (1962)]

Temperature	Property				
	Ultimate Tensile Strength (ksi)	Yield Strength (0.2% effect) (ksi)	Elongation (total) (%)	Modulus of Elasticity (100 psi)	Hardness (VHN)
Room temp	56–96	24–38	6–12	22–29	255
570°F (299°C)	35	18	33–49	16	104
930°F (499°C)	11	5–7	44–61	14	46

A.2 Chemical Properties of Uranium Metal

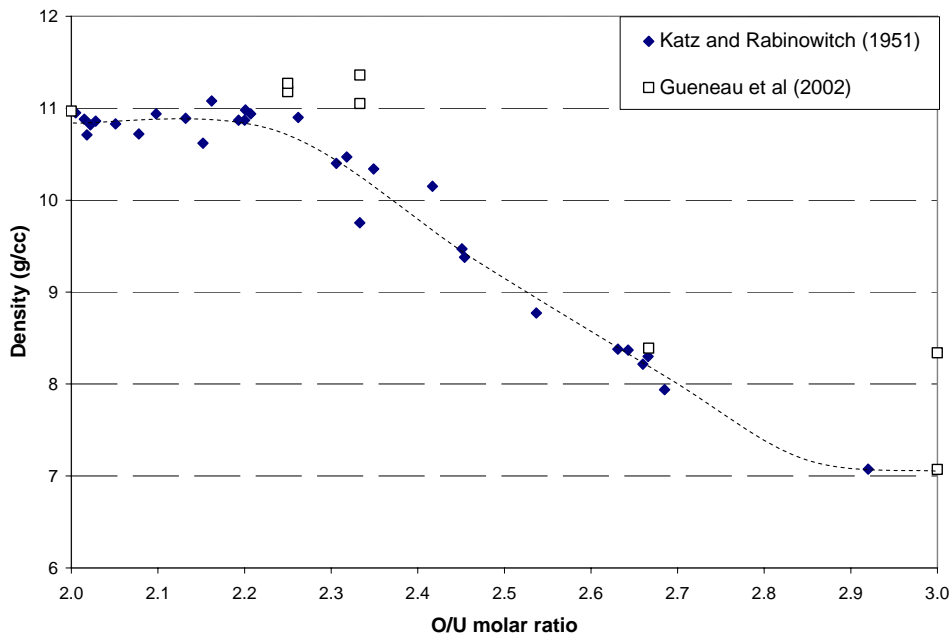


Figure A.1 Density Change in the UO_2 to U_3O_8 transition.

Table A.2 Selected Chemical Properties of Uranium Metal [Klein (1962)]

Density at 25°C, g/cm³				
High purity	19.05 ± 0.02			
Wrought, variable purity	18.7 – 19.1			
Allotropic transformation temperature, °C				
Alpha (α) ↔ beta (β)				
Equilibrium	662 ± 3			
Minimum for slow heating	666 ± 2			
Maximum for slow heating	658 ± 5			
Beta (β) to gamma (γ)				
Equilibrium	774 ± 4			
Minimum for slow heating	776 ± 3			
Maximum for slow heating	772 ± 5			
Freezing temperature	1132 ± 1			
Vapor pressure				
P, mm Hg	K		°C	
10 ⁻⁶	1598		1325	
10 ⁻⁵	1713		1440	
10 ⁻⁴	1853		1580	
10 ⁻³	2013		1740	
10 ⁻¹	2433		2160	
760	4086		3813 (bp)	
Heats and entropies of transformation				
Transformation	Temperature		ΔH or Q, kcal/mole	ΔS, cal/mole/K
	K	°C		
Alpha → beta	939	666	0.680 – 9.712	0.724 – 0.758
Beta → gamma	1049	776	1.142 – 1.164	1.080 – 1.110
Gamma → liquid	1405	1132	~4.7	3.3
Liquid → vapor	---	---	93 – 107	---
Solid → vapor	---	---	117	---

Appendix B - Data for Figure 2.1

The basis for the data comes from Baker et al (1966) page 33 which is the foundation for most comparisons using specific area. The actual data is presented for reproducibility of the figure, since the general trend of the Figure as summarized by Baker et al is typically copied as opposed to recreated.

Table B.1 Excerpted Data from Table 1 of Baker et al. (1966)

Specific Area (cm ² /g)	Ignition Temp (C)	
	Oxygen	Air
0.280	640	
0.334	615	700
0.396	595	650
0.396	595	
0.396	575	
0.790	540	
0.894	565	655
1.060	530	
1.220	570	
1.410	510	
2.020	385	
2.590	460	525
2.630	470	
3.100	390	
4.670	435	475
4.680	385	385
5.180	410	
5.300	385	
8.500	380	390
49.000	335	350
121.000	315	395